JGR Solid Earth

RESEARCH ARTICLE
10.1029/2025JB032208

Range-Parallel Extension of the Andes in the 2020 Mw 5.7 Humahuaca Earthquake

Simon Orrego[1], **Juliet Biggs**[1], **Sam Wimpenny**[1], **and Yasser Maghsoudi**[2]

[1]COMET, School of Earth Sciences, University of Bristol, Bristol, UK, [2]COMET, Department of Earth and Environmental Sciences, University of Exeter, Exeter, UK

Key Points:

- The M_w 5.7 Humahuaca earthquake occurred on a buried normal fault perpendicular to the range front
- The M_w 5.7 Humahuaca earthquake provides a well-documented example of range-parallel extension outside Tibet
- Regional topography, slip vectors and GNSS data together suggest that gravitational spreading and/or strain partitioning may cause local extension

Supporting Information:

Supporting Information may be found in the online version of this article.

Correspondence to:

S. Orrego,
zy22448@bristol.ac.uk

Citation:

Orrego, S., Biggs, J., Wimpenny, S., & Maghsoudi, Y. (2025). Range-parallel extension of the Andes in the 2020 Mw 5.7 Humahuaca earthquake. *Journal of Geophysical Research: Solid Earth*, *130*, e2025JB032208. https://doi.org/10.1029/2025JB032208

Received 13 JUN 2025
Accepted 30 NOV 2025

Author Contributions:

Conceptualization: Simon Orrego, Juliet Biggs, Sam Wimpenny
Data curation: Simon Orrego
Formal analysis: Simon Orrego
Funding acquisition: Juliet Biggs
Methodology: Simon Orrego, Juliet Biggs, Sam Wimpenny
Project administration: Juliet Biggs
Resources: Juliet Biggs
Software: Simon Orrego, Juliet Biggs, Sam Wimpenny, Yasser Maghsoudi
Supervision: Juliet Biggs, Sam Wimpenny
Validation: Simon Orrego
Visualization: Simon Orrego
Writing – original draft: Simon Orrego

Abstract Normal-faulting earthquakes in mountain ranges provide important constraints on the dynamics of mountain building. To date, well-documented examples of range-parallel extension come primarily from the Tibetan Plateau, limiting our ability to test different models for its cause. Here, we investigate a new example of range-parallel extension: the 2020 M_w 5.7 Humahuaca earthquake in the Andes of Argentina. We combine observations from InSAR displacement time-series and body-waveform seismology to constrain a source model for the earthquake. We find the faulting accommodated range-parallel extension at 6 km depth with an epicenter ~50 km west of the Andes range front. Combining our new source model with existing GNSS and earthquake slip-vector measurements, we suggest that range-parallel extension in the Andes may result from one or more of the following mechanisms: (a) divergent thrust-faulting caused by gravitational spreading, (b) localized transtension in step-overs between range-parallel strike-slip faults accommodating trench-parallel shear, or (c) localized extension at the edges of rigid blocks rotating about vertical axes. Unlike the Tibetan Plateau, there is no evidence for widespread lateral extrusion of crust. All three viable models suggest the potential for further moderate-magnitude earthquakes within the Eastern Cordillera, which are currently not included as sources of earthquakes in probabilistic seismic hazard models of the Andes.

Plain Language Summary Mountain belts form due to compression and thickening of the Earth's buoyant crust. However, some mountain belts experience earthquakes that indicate the crust is extending and thinning. The direction of this extension can be either roughly parallel, or roughly perpendicular, to the trend of the mountain belt and is an important indicator of the forces causing the mountain belt to deform. Here, we document an earthquake in the central Andes of Argentina that caused extension parallel to the mountain belt. Previously, this type of earthquake has been documented mainly on the Tibetan Plateau. We suggest that, in the central Andes, the extension can either be caused by the weaker mountainous region spreading out over the strong South American continent, or by shear across the mountains due to the oblique angle at which the Nazca Plate converges with South America. Extensional earthquakes within the Andes are not included in existing seismic hazard analyses, meaning the ground shaking in the eastern Andes may be underestimated.

1. Introduction

Normal faulting within the interior of a mountain range can occur at the same time as thrust faulting along its margins, and the spatial and kinematic relationship between the two types of faulting is a key indicator of the forces controlling mountain building (England & Houseman, 1988; Molnar & Lyon-Caen, 1988). Two end-member patterns of normal and thrust faulting have been observed in mountain belts. In the Peruvian Andes, Albania, south-eastern Tibet and western Pamir, normal faults strike parallel to the mountain range front (Figure 1) and accommodate extension parallel to the slip vectors of thrust faults along their margins ("range-perpendicular" extension) (Copley et al., 2009; Copley & Mckenzie, 2007; Dalmayrac & Molnar, 1981; Schurr et al., 2014; Wimpenny et al., 2018; Zubovich et al., 2016). In contrast, in the Tibetan Plateau normal faults strike perpendicular to the mountain range front (Figure 1) and accommodate extension perpendicular to the slip vectors of thrust faults along its margin ("range-parallel" extension) (Armijo et al., 1986; Molnar & Lyon-Caen, 1989; Tapponnier et al., 1981).

Range-parallel extension in the Tibetan Plateau has been explained by at least four different models, including: (a) convective removal of a thick, dense Tibetan lithospheric mantle and gravitational collapse (e.g., England & Houseman, 1989), (b) gravitational spreading of a viscous Tibetan crust over a rigid Indian foreland (e.g., Copley et al., 2011), (c) eastward extrusion and lateral escape of Tibetan crust toward an area of weak crust in south-

Writing – review & editing:
Simon Orrego, Juliet Biggs,
Sam Wimpenny, Yasser Maghsoudi

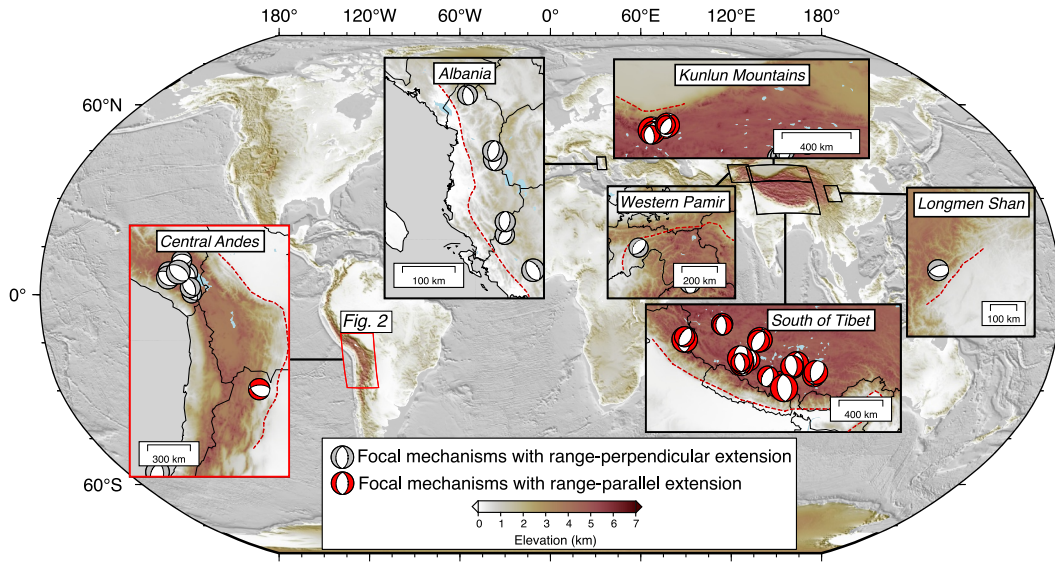

Figure 1. Global distribution of normal-faulting earthquakes (depth <20 km, and M_w > 4.5) in mountain belts. The inset panels show individual mountain belts and shallow normal-faulting earthquakes from gWFM v1.2 (Wimpenny & Watson, 2020) and global CMT catalogs (Ekström et al., 2012), with focal mechanisms in gray representing earthquakes accommodating range-perpendicular extension and focal mechanisms in red accommodating range-parallel extension. The focal mechanism in Longmen Shan was obtained from Li et al. (2019). The red dashed lines represent the range front.

eastern Tibet (e.g., Cook & Royden, 2008), and (d) strain partitioning due to oblique convergence between India and southern Tibet (e.g., Styron et al., 2011). Our ability to differentiate between these models is limited by a lack of examples of range-parallel extension in tectonic settings other than the Tibetan Plateau. However, the four models lead to significantly different interpretations of the geological evolution of Tibet, and therefore also other mountain belts in both active and ancient settings with evidence for range-parallel extension.

In this study, we describe a moderate-magnitude earthquake that accommodates range-parallel extension outside Tibet (Figure 2). The M_w 5.7 earthquake occurred in 2020 near Humahuaca in the high Andes of northern Argentina. We use InSAR time-series measurements and body-wave seismology to accurately determine the location and source model of the Humahuaca earthquake. We then place the earthquake's kinematics into the wider context of the active tectonics of the central Andes using slip vectors and GNSS velocities. Finally, we discuss the implications of our findings for the kinematic and dynamical controls on range-parallel extension and the possible seismic hazard in the eastern Andes.

2. Tectonic Background

2.1. Tectonic Setting of the 2020 M_w 5.7 Humahuaca Earthquake

The Andes mountains began uplifting in the mid-late Cretaceous (120–70 Ma) (Coira et al., 1982; Horton, 2018). Today the pattern of thrust-faulting earthquakes indicates that shortening and uplift is concentrated along the margins of the mountain range (Devlin et al., 2012), although with varying styles of shortening along-strike (Kley et al., 1999). In contrast, the interior of the Andes between southern Peru and Argentina consists of a low-relief plateau known as the Altiplano-Puna where there have been few earthquakes and there is only subtle geomorphological evidence for active faulting (Allmendinger et al., 1989; Devlin et al., 2012; Lamb, 2000; Wimpenny et al., 2020), meaning the kinematics of deformation and seismic hazard in the Altiplano-Puna plateau are poorly defined.

The 2020 M_w 5.7 Humahuaca earthquake occurred in the Cianzo region of the northwestern Argentinian Andes (Figure 3), close to the boundary between the Puna plateau and the eastern range front. Preliminary estimates of the earthquake's focal mechanism suggest it was associated with ~E–W striking normal-faulting in the shallow crust (Ekström et al., 2012; Figures 3a and 3b), though epicentral location estimates for the event vary by up to ~40 km, and depth differences by up to ~10 km, between earthquake catalogs (Figure 3). The mechanism of this

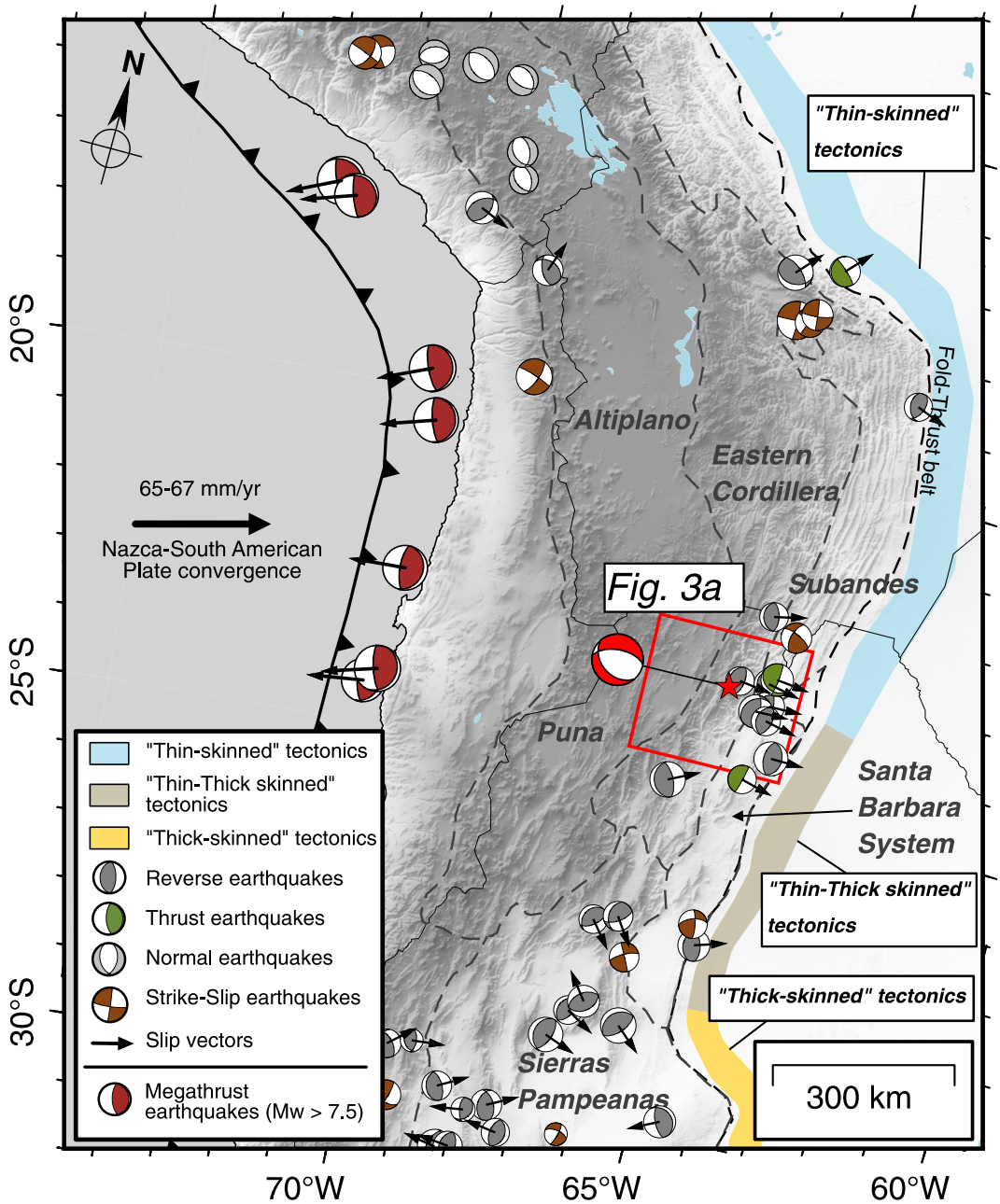

Figure 2. Tectonic setting of the 2020 Humahuaca earthquake. The map is in oblique Mercator projection about the Euler pole of the Nazca-South American convergence from Jarrin et al. (2023). Megathrust earthquakes are from the Global CMT catalog (Ekström et al., 2012). Other focal mechanisms are from gWFM v1.2 (Wimpenny & Watson, 2020) and the Global CMT catalog. The dashed gray lines show the morphotectonic boundaries in the central Andes, while solid thin black lines show the boundaries of the countries. Areas of thin- and thick-skinned tectonic shortening are taken from Kley et al. (1999).

earthquake was unexpected, as all other crustal seismicity at the edge of the Puna has been ~N–S striking thrust-faulting earthquakes (Figure 3a). In addition, normal-faulting seismicity elsewhere in the Altiplano-Puna accommodates mainly range-perpendicular extension (Cabrera & Sébrier, 1998; Devlin et al., 2012; Wimpenny et al., 2018), not range-parallel extension as suggested by the preliminary mechanism for the 2020 Humahuaca earthquake (Figure 3).

The 2020 Humahuaca earthquake epicenter lies adjacent to a transition in the geomorphology and crustal seismicity along the range front of the Andes. North of 23° S is the Bolivian sub-Andes, where there have been few

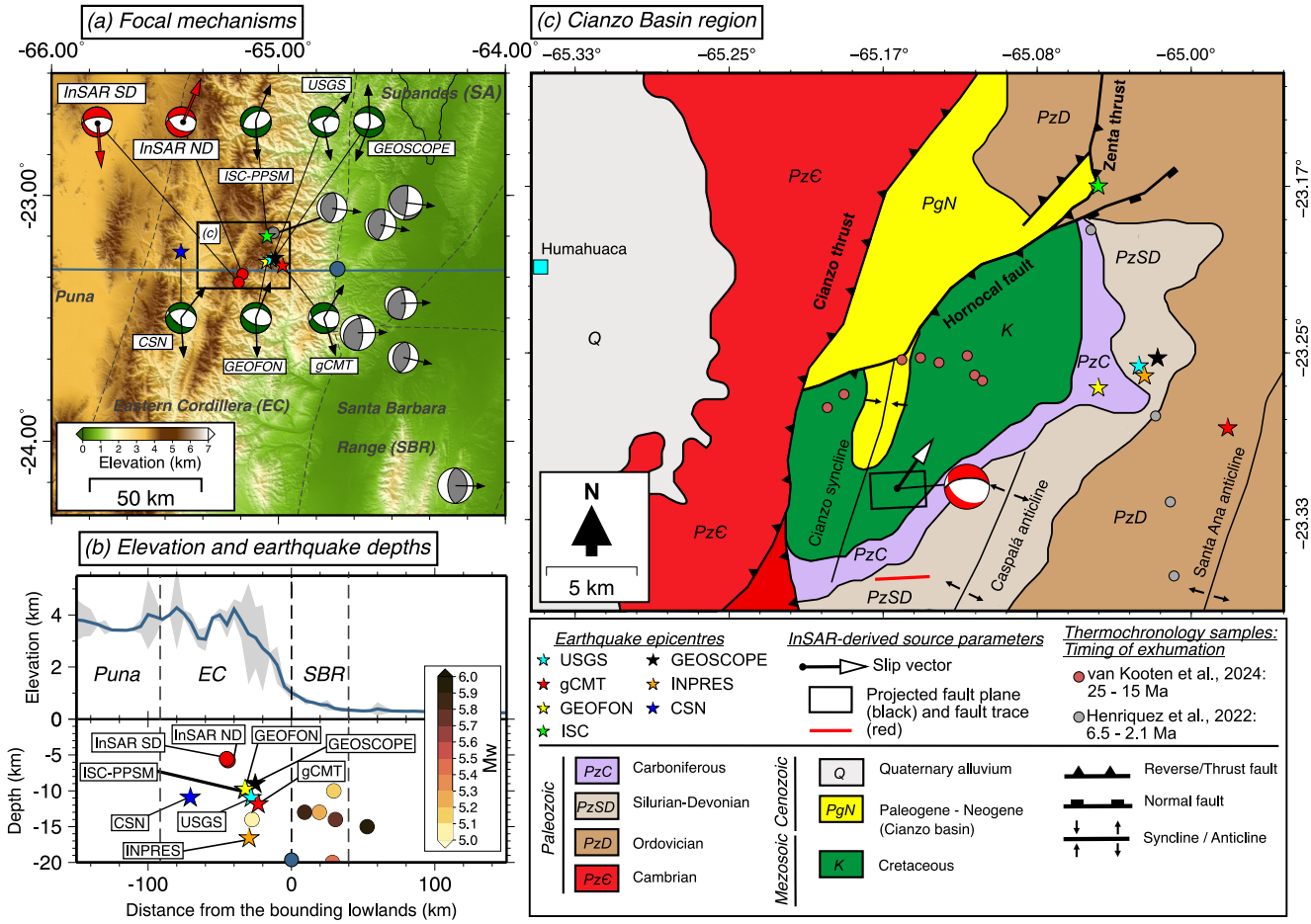

Figure 3. Overview of the focal mechanism, epicentral location and tectonic setting of the 2020 Humahuaca earthquake. (a) Focal mechanism solutions for the Humahuaca earthquake: green beachballs: ISC-PPSM (Garth et al., 2023), USGS, GEOSCOPE (Leroy et al., 2024), CSN (Barrientos & Team, 2018), GEOFON (Quinteros et al., 2021), gCMT (Ekström et al., 2012); red beachballs: InSAR-derived solutions (ND: North-dipping, SD: South-dipping). Gray beachballs: other west-dipping reverse-faulting earthquakes along the adjacent range front. Also shown are slip vectors for both nodal planes of each mechanism. The blue line indicates the location of the topography profile shown in (b), centered on the blue dot. (b) Topographic cross-section passing through the epicentral region. The bottom panel displays the earthquakes in (a), with our 2020 Humahuaca earthquake solutions marked by red dots. (c) Simplified geological map of the epicentral region, adapted from Siks and Horton (2011). Thermochronological sampling locations from Henriquez et al. (2022) and van Kooten et al. (2024) are indicated by circles. The map-view of our InSAR-derived solution for north-dipping fault plane and its surface projection are shown as a black box and red line, respectively.

thrust-faulting earthquakes, seismicity is confined to <20 km depth in the foreland crust (Devlin et al., 2012; Fernández et al., 2024) and the geomorphology is characterized by linear anticlinal ridges believed to be underlain by imbricate, foreland-verging thrusts (Kley et al., 1999). South of latitude 27° S is the Sierra Pampeanas, where the whole foreland crust is currently breaking in frequent reverse and strike-slip faulting earthquakes (Alvarado & Beck, 2006; Assumpção & Araujo, 1993; Kadinsky-Cade et al., 1985; Meigs & Nabelek, 2010) and the geomorphology is characterized by isolated basement uplifts (Kley et al., 1999). We refer to these different styles of shortening as thin-skinned and thick-skinned, respectively (Figure 2).

Active normal faulting near Humahuaca is likely to be a relatively recent feature—until ~2 Ma the Cianzo region was undergoing crustal shortening (Henriquez et al., 2022; Siks & Horton, 2011; van Kooten et al., 2024). The two major geological faults in the area are the Hornocal fault and Cianzo thrust (Figure 3c). The NE–SW striking Hornocal fault was formed during the Cretaceous as large SE-dipping normal fault, that controlled the sedimentation during opening of the Salta rift system (Kley et al., 2005). Subsequent east-west Andean compression led to the reactivation of the Hornocal fault as an oblique reverse fault (Kley et al., 2005; Siks & Horton, 2011). Apatite thermochronology indicates that exhumation in the hanging wall of the Hornocal fault, caused by its reactivation, occurred between 24 and 2 Ma (Henriquez et al., 2022; van Kooten et al., 2024) (location of the samples in Figure 3c). The N–S striking Cianzo thrust marks the western boundary of the Cianzo basin

(Henriquez et al., 2022; Siks & Horton, 2011). Cross-cutting relationships require that slip of the Cianzo thrust postdates slip on the Hornocal fault (Henriquez et al., 2022; Siks & Horton, 2011; van Kooten et al., 2024), which indicates that it occurred in the late stages of Hornocal fault reactivation, between 6 Ma and 2 Ma. However, it is not clear whether the Cianzo thrust is a reactivated structure or formed during Andean compression (van Kooten et al., 2024). The Cianzo syncline, a NNE–SSW trending overturned asymmetric fold cored by Paleogene-Neogene sediments (Siks & Horton, 2011), provides further evidence for Neogene-age shortening in the Cianzo region.

Although no normal faulting earthquakes have previously been documented in this region, several studies have reported geomorphological evidence of Quaternary normal and strike-slip faulting in the Puna plateau and Eastern Cordillera nearby (Allmendinger et al., 1989; Daxberger & Riller, 2015; Marrett et al., 1994; Schoenbohm & Strecker, 2009; Zhou et al., 2013). The nearest example comes from ∼25 km west of Humahuaca, where Marrett et al. (1994) identified evidence for strike-slip faulting in alluvial deposits inferred to be of Quaternary age. Fault-striae analysis revealed older thrust movement on the same fault in rocks dated late Miocene-early Pleistocene. Zhou et al. (2013) was able to more accurately date normal faults 300 km SSW of Humahuaca that preserved <10 m-high offsets in ∼1 Ma lava domes that accommodate NE–SW to NNE–SSW extension around the southeastern margin of the Puna plateau. Normal faults with more significant offsets of ∼200 m have been mapped in the Fiambalá Basin in the southern Puna plateau that accommodate NNW–SSE extension (Schoenbohm & Strecker, 2009). These observations tentatively suggest that strike-slip and normal faulting may be more widespread in the Puna plateau than suggested from the recent seismicity, but that these faults are either not recently active or have low slip rates.

3. Source Model of the 2020 Humahuaca Earthquake

In this section, we re-analyze the source mechanism and location of the Humahuaca earthquake using a combination of seismology and satellite geodesy. We undertake this re-analysis because the locations and source mechanisms of $M_w < 6.0$ earthquakes derived from semi-automated methods can, on rare occasion, be erroneous (Blom et al., 2022; Craig et al., 2023; Ferreira et al., 2011; Weston et al., 2012; Wimpenny & Watson, 2020). For example, seismological re-analysis of four M_w 5–6 earthquakes in the Tibetan plateau contained within the gCMT catalog revealed errors of up to 60 km in the centroid depths, which also led to erroneous focal mechanisms for these events (Craig et al., 2023). Furthermore, previous studies have identified significant discrepancies between seismic catalogs and geodetic inversions for moderate-sized earthquakes, particularly regarding epicentral locations (up to 40–50 km differences) and source geometries (strike differences up to ∼30°) (Weston et al., 2014; Wimpenny & Watson, 2020). In particular, the complex velocity structure of the South American subduction zone (e.g., Gao et al., 2021; Koulakov et al., 2006) creates a systematic westward bias in the locations of earthquakes off the coast (Pritchard et al., 2006; Weston et al., 2014), and an eastward bias for earthquakes in the foreland region. This is because global seismic catalogs utilize 1-D velocity models in their location procedures, which do not capture the 3-D velocity structure.

In this section, we first describe our modeling of the 2020 Humahuaca earthquake using long-period body-waveform seismology, which is particularly sensitive to the focal mechanism and centroid depth of the earthquake. We then describe our modeling of the earthquake using InSAR time-series analysis measurements, which is sensitive to the location and geometry of the fault plane that ruptured.

3.1. Body-Waveform Seismology

We first modeled the focal mechanism, centroid depth and source-time function of the 2020 Humahuaca earthquake to determine its source parameters and their uncertainties. We used long-period *P* and *SH* waveforms measured on vertical- and transverse-component seismograms with epicentral distances between 30° and 90°. We followed the standard approach described in detail by Nabelek (1984) and adapted by McCaffrey and Abers (1988), which we summarize briefly below.

We picked 20 *P* and 16 *SH*-wave arrivals from the broadband seismograms with high signal-to-noise ratio to provide good azimuthal coverage of the focal sphere. We then filtered the seismograms to periods between 15 and 100 s to reproduce the response of a WWSSN 15–100 instrument. Within this frequency range, the earthquake can be treated like a point source. We manually realigned the seismograms to *P* and *SH*-wave picks making the inversion insensitive to uncertainties in source location. We then performed iterative, weighted least squares

Table 1
Comparison of the 2020 Humahuaca Earthquake Source Parameters From Seismology and InSAR-Derived Best-Fit Solutions

Model	Strike	Dip	Rake	Depth (km)[a]	Length (km)	Width (km)	M_0 (N m)	RMSE (mm)	Location[b]
gCMT	252°	58°	−108°	12	–	–	4.92×10^{17}	–	64.980°W, 23.290°S
USGS	258°	61°	−114°	11.5	–	–	5.80×10^{17}	–	65.028°W, 23.259°S
CSN	267°	41°	−123°	11	–	–	–	–	65.430°W, 23.230°S
GEOFON	269°	35°	−109°	10	–	–	–	–	65.050°W, 23.270°S
GEOSCOPE	291°	43°	−72°	9.0	–	–	–	–	65.018°W, 23.255°S
ISC-PPSM	234°	39°	−109°	10	–	–	–	–	65.050°W, 23.169°S
InSAR ND	266^{+5}_{-4}	58^{+3}_{-4}	-113^{+18}_{-12}	$5.8^{+0.4}_{-0.4}$	$3.0^{+0.9}_{-0.1}$	$3.7^{+1.3}_{-0.7}$	3.46×10^{17}	3.3	65.160°W, 23.300°S
InSAR SD	123^{+10}_{-5}	30^{+5}_{-1}	-59^{+14}_{-10}	$5.2^{+0.6}_{-0.4}$	$4.5^{+0.2}_{-1.3}$	$4.5^{+0.3}_{-1.5}$	3.49×10^{17}	4.0	65.187°W, 23.330°S
InSAR ind. interferograms	225^{+39}_{-1}	31^{+21}_{-1}	-135^{+28}_{-25}	$4.5^{+1.7}_{-0.5}$	$6.3^{+0.8}_{-3.1}$	$9.3^{+1.1}_{-5.3}$	4.01×10^{17}	11.95	65.165°W, 23.240°S
gCent[c]	250°	68°	−145°	5.3	4.2	0.9	5.28×10^{17}	–	65.148°W, 23.317°S
Teleseismic BWF ND	269° (250°–290°)	51° (40°–65°)	−114° (−130°– −100°)	8.0 (5–13)	–	–	4.02×10^{17}	–	–
Teleseismic BWF SD	124°	45°	−63°	8.0	–	–	4.02×10^{17}	–	–

Note. Centroid and hypocentral/epicentral locations and depths are distinguished where applicable. The uncertainties for InSAR models are defined by the 95% confidence intervals of the posterior probability density functions. Seismic moment (M_0) is calculated using a shear modulus of 30 GPa. BWF represent the long-period body-waveform solution. ND, north-dipping, SD, south-dipping, RMSE, root mean square error. [a]Depths from gCMT, GEOFON, GEOSCOPE, and gCent represent centroid depths; depths from USGS, CSN, and ISC-PPSM correspond to hypocentral depths. InSAR depths represent the centroid depth of the uniform-slip fault plane. [b]Locations from gCMT, GEOFON, GEOSCOPE, and gCent represent centroid location; locations from USGS, CSN, and ISC-PPSM represent epicentral (hypocentral) locations. The InSAR locations correspond to the surface projection of the mid-point of the fault plane for a uniform slip model. [c]Geodetic earthquake catalog by Shea and Barnhart (2022), which employs individual interferograms to resolve source parameters for this event.

inversions for the best-fitting strike, dip, rake, centroid depth, source-time function and moment magnitude of the Humahuaca earthquake using the computer program MT5 (Zwick et al., 1994). We do not invert for the centroid longitude or latitude as long-period waveforms are insensitive to small-scale heterogeneity in the source region velocity structure (Taymaz et al., 1990). Therefore, we used a simple 1-D crustal velocity structure to generate the synthetic seismograms with V_p = 6.5 km/s, V_s = 3.7 km/s, and a density = 2,800 kg/m^3 (Schurr et al., 1999).

The best-fit solution corresponds to a normal fault with a strike of 269°, dip of 51°, and rake of −114°, a centroid depth of 8 km, and a seismic moment of 4.02×10^{17} N m (M_w 5.74; see waveform fits in Figure S2 in Supporting Information S1 and Table 1). To assess the uncertainties associated with each source parameter, we fixed each parameter over a range of values and performed inversions in which the remaining parameters were allowed to vary. We define the upper and lower bounds on each parameter to be where there were visually poor fits between the synthetics and the observed waveforms. Using this method we estimate the strike is constrained to between 250° and 290°, the dip between 40° and 65°, and the rake between −130° and −100° (Figure 7). Additionally, we determined that centroid depths exceeding 13 km do not provide a good fit to the observed SH waveforms.

We tested the effects of including a two-layer velocity model consisting of a sedimentary layer extending to 2 km depth, characterized by V_p = 4.8 km/s, V_s = 2.64 km/s, and a density = 2,500 kg/m^3, underlain by a crystalline basement with the same velocity structure of the uniform model. The results show minimal effect on the best-fit source parameters, varying 1° in strike, no variations in dip, and 2° in rake, with a seismic moment

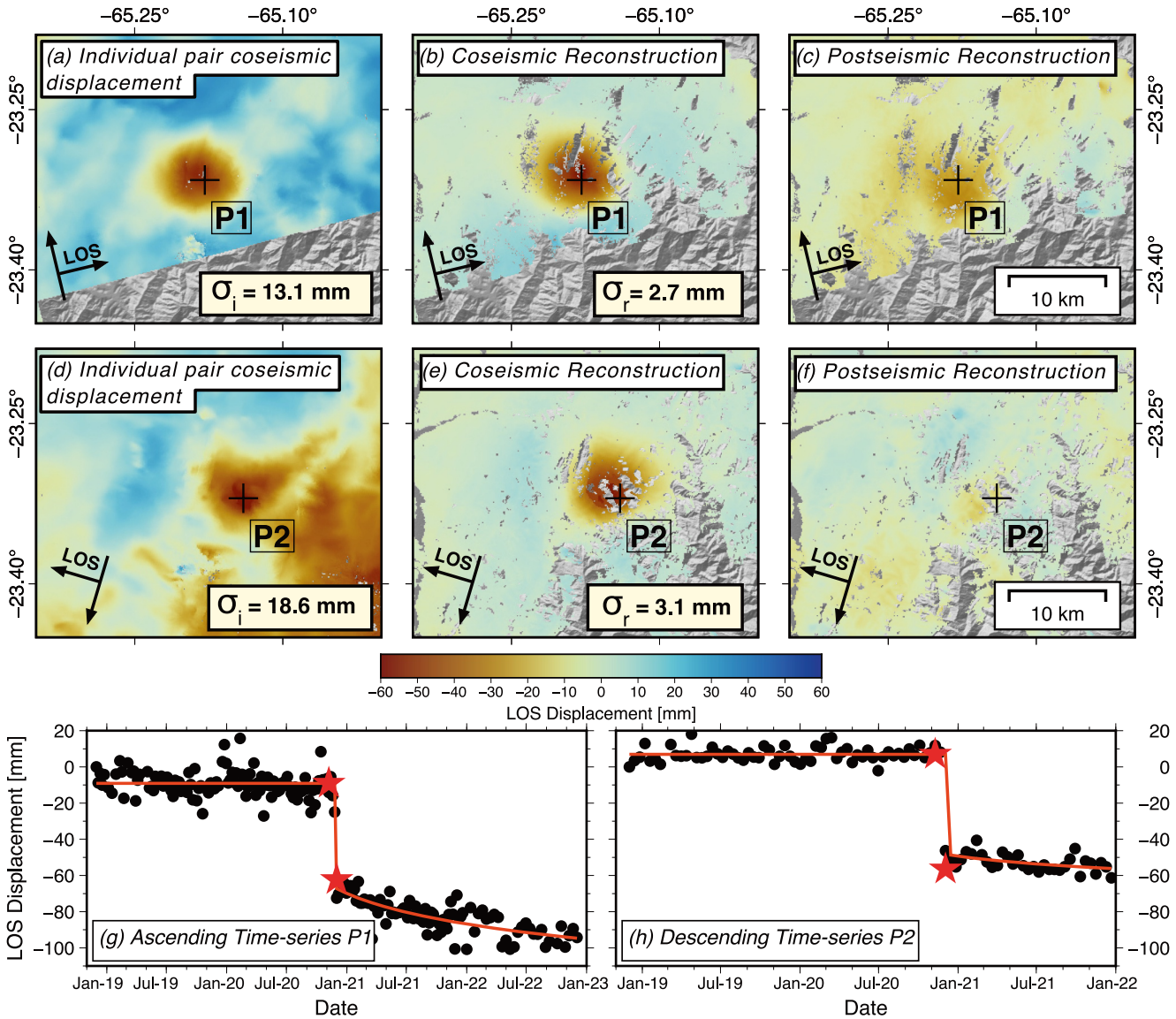

Figure 4. InSAR-derived surface displacement measurements for the 2020 Humahuaca earthquake and its subsequent postseismic deformation (a-c) show the ascending-track observations for individual coseismic displacement pair 07 November 2020–01 December 2020 (a), the reconstructed coseismic displacement (b) and the reconstructed cumulative postseismic displacement (c) (d–f) show descending-track observations for individual coseismic displacement pair 09 November 2020–03 December 2020 (d), reconstructed coseismic displacement (e) and reconstructed cumulative postseismic displacement (f). (g) and (h) show displacement time-series for individual pixels at P1 and P2 as black circles. The best-fitting model using Equation 1 for each time-series is represented by an orange line. The red stars represent the LOS displacement for P1 and P2 measured from the individual InSAR-derived coseismic displacements.

of 4.1 × 10^{17} N m. We further tested a modified velocity structure representative of crystalline basement in the Eastern Cordillera down to 20 km depth with V_p = 6.2 km/s, V_s = 3.6 km/s, and a density = 2,800 kg/m^3 (Gao et al., 2021). The V_p/V_s ratio is 1.72, corresponding to a Poisson's ratio (ν) of 0.25, which is consistent with the value adopted in our elastic dislocation modeling (Section 3.3). The results indicate minor variations in the best-fit source parameters, with differences of 1° in strike, dip, and rake, and a seismic moment of 3.84 × 10^{17} N m. These results demonstrate that the uniform velocity model is consistent with the two-layered model, with differences well within the range of uncertainty.

3.2. InSAR

3.2.1. InSAR Methodology

Measuring the surface displacement from moderate-magnitude earthquakes (M_w 5–6) using InSAR can be challenging, as atmospheric noise can obscure the low-amplitude deformation signals (Luo et al., 2021; Yu, Li, Chen, & Hu, 2018). To overcome this limitation, we use InSAR time-series analysis as a means of suppressing atmospheric noise relative to deformation signals (Daout et al., 2019, 2020; Guns et al., 2022; León-Ibáñez & Delgado, 2025; Liu et al., 2021).

We produced InSAR time-series spanning the 2 years either side of the 2020 Humahuaca earthquake using Sentinel-1 images. Due to limitations related to the Sentinel-1B failure and the lack of Sentinel-1A acquisitions over the Humahuaca region, we were only able to generate InSAR-derived displacements up to 1 year after the earthquake for the descending track. We used the LiCSAR processing chain (Lazeckỳ et al., 2020) to generate 1,273 ascending-track and 461 descending-track interferograms in both short and long temporal baselines (≤180 days). We removed the topographic contribution to phase using the GLO-30 Copernicus Digital Elevation Model (DEM) and we multi-looked the interferograms by factors of 20 times in range and 5 times in azimuth to generate a pixel size of ∼100 m, and filtered them using the adaptive phase filter from Goldstein and Werner (1998). We then applied GACOS corrections to remove some atmospheric contributions to phase (Yu, Li, Penna, & Crippa, 2018). We carry out the InSAR time-series processing using the New Small Baseline Subset (NSBAS) algorithm (Doin et al., 2011) implemented in LiCSBAS package (Morishita et al., 2020). The result is a time-series of ground displacement projected into the satellite line-of-sight (LOS) at every pixel. Additional information about processing and the interferogram network is provided in the Table S1 and Figure S1 in Supporting Information S1.

Residual atmospheric noise within the time-series will not be consistent between different epochs, while real signals from coseismic and postseismic deformation should follow a simple temporal evolution. We therefore took a parametric approach to reconstructing the coseismic and postseismic surface displacement fields from the InSAR time-series measurements (Daout et al., 2019, 2020; Guns et al., 2022; Jolivet & Simons, 2018; Liu et al., 2021). We model the surface displacement $D(t)$ at each pixel using Equation 1:

$$D(t) = H(t - t_{eq})\left[C + A \cdot \ln\left(1 + \frac{t}{\tau}\right)\right] + b \quad (1)$$

Equation 1 includes a Heaviside step function, $H(t - t_{eq})$, at the time of the earthquake t_{eq} to account for instantaneous coseismic displacement, and a logarithmic decay after the earthquake with relaxation time τ to capture the postseismic displacement plus a constant offset b. C represents the coseismic displacement at time of the earthquake t_{eq} and A the amplitude of the postseismic displacement. To assess the magnitude of the long-term background deformation in the study area, we fitted a planar trend to the LOS velocities over the entire InSAR coverage area for the two years preceding the 2020 Humahuaca earthquake. The resultant velocity field is dominated by motion away from the satellite, and shows spatial variations of up to 2.3 and 0.3 mm/yr over a distance of ∼50 km for ascending and descending tracks, respectively (Figure S3 in Supporting Information S1). These values are consistent with estimates of vertical velocity rates from GNSS, which are predominantly negative and differ by 1.62 ± 0.47 mm/yr across ∼110 km in the eastern Andes (Figueroa et al., 2021). Therefore, we did not include a contribution from the long-term velocity due to back-arc shortening and plate motion in our time-series fitting approach, as it contributes <6 mm of cumulative displacement to the 3-year-long InSAR time-series over the 50 km-wide study area. Additionally, we did not estimate seasonal variations, as these effects are minimal and fall within the background noise levels of the InSAR time-series. We solved for the constants in Equation 1 for every pixel using a non-linear least squares inversion.

A limitation with this approach is that the characteristic timescale for postseismic relaxation τ is poorly constrained by the data and trades-off against other parameters. We therefore select the value of τ prior to solving for the parameters in Equation 1. Specifically, we stack the observed postseismic displacement time-series from 496 manually defined pixels located at the peak of postseismic deformation (Figure 5) and perform inversions with τ fixed in Equation 1 over a range of 5–1,200 days. The optimal τ is chosen as the value that minimizes the root-mean-square error (RMSE) of the stacked time-series (Figure 5b). We then fix the optimal τ and use it across all pixels in the inversion, thereby avoiding the need for an initial guess during parameter estimation.

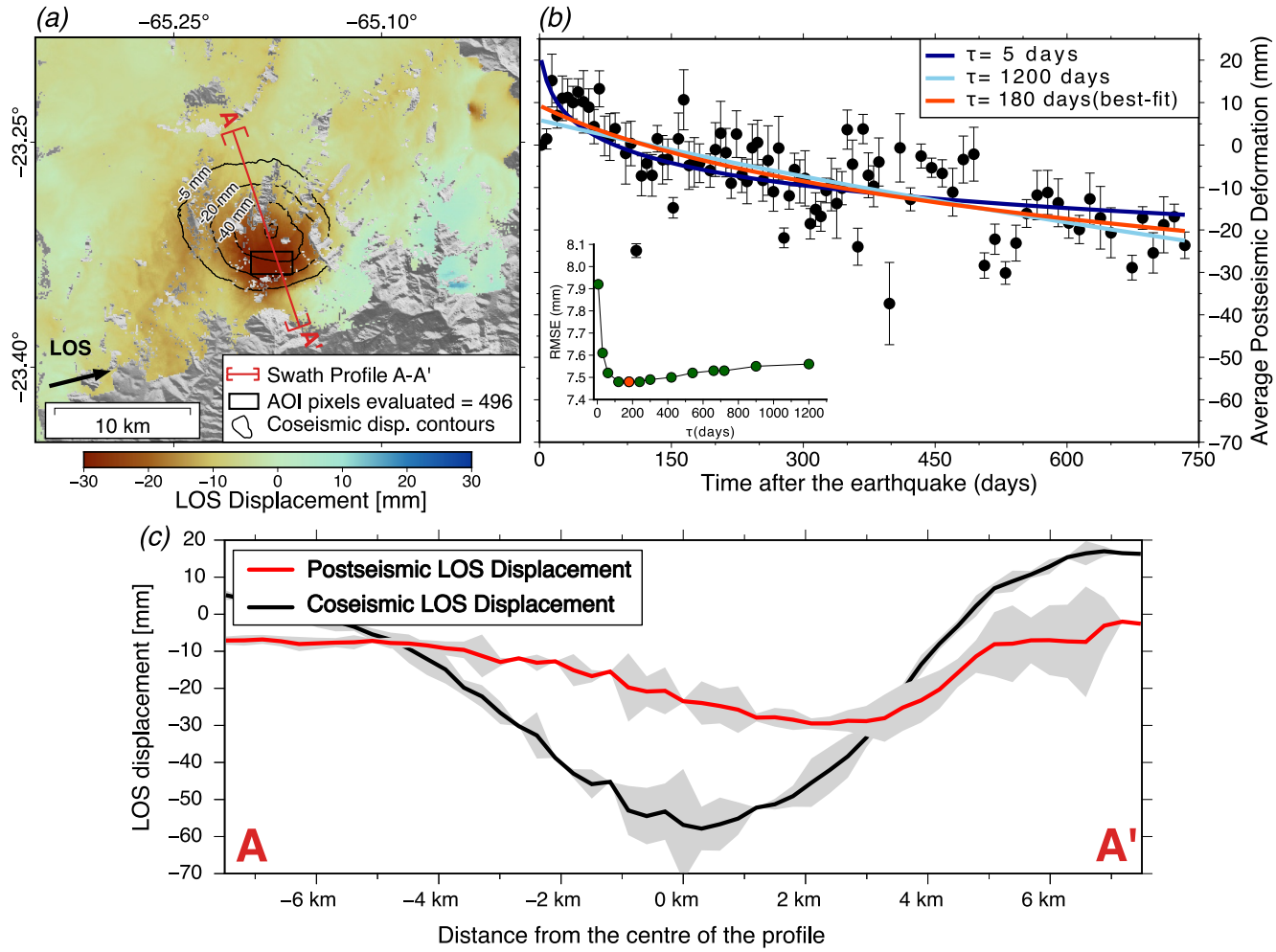

Figure 5. Pattern of postseismic deformation following the 2020 Humahuaca earthquake. (a) Reconstructed postseismic deformation for the period between 01 December 2020 and 03 December 2022 for the ascending track. The black contours show the coseismic displacement. (b) Fit between the observed time-series and Equation 1 using three different relaxation times τ. The time-series is constructed from the average LOS of pixels inside the black box in (a). The orange line represents the best-fitting model with $\tau = 180$ days. The error bars represent 2-standard deviation of pixel LOS in the black box in (a). Inset plot shows the reconstruction model misfit for various fixed τ values to Equation 1. The orange dot indicates the best-fit solution. (c) 500-m wide profiles extracted from the coseismic and postseismic LOS displacement fields from the ascending track along A–A′ in (a). The gray swath shows the maximum and minimum LOS displacement values for each distance within the profile box. RMSE=Root-mean-square error.

3.2.2. InSAR Observations

Figure 4 shows selected InSAR-derived coseismic displacements from individual interferograms and our reconstructed coseismic and postseismic surface displacements for ascending and descending tracks. Both the individual and the reconstructed displacements show a smooth lobe of negative line-of-sight (LOS) coseismic displacement up to ∼5–6 cm in ascending and descending tracks, which is consistent with slip on a buried dip-slip fault. The shape of the displacement lobe is better defined in the reconstructed deformation fields compared to the individual interferograms, which are more affected by atmospheric phase delays.

To quantitatively assess the noise reduction resulting from our time-series reconstruction, we calculated the change in the standard deviation of pixel values in non-deforming areas of the surface displacement field, which is defined as: $\Delta\sigma = \frac{\sigma_i - \sigma_r}{\sigma_i}$, where σ_i is the standard deviation of the individual interferogram and σ_r is the standard deviation of the reconstruction (Figure S4 in Supporting Information S1). Noise in individual interferograms fields σ_i was ∼13 mm and ∼19 mm for ascending and descending tracks, respectively, and we found a noise reduction $\Delta\sigma$ of 79% for the ascending track and 83% for descending track.

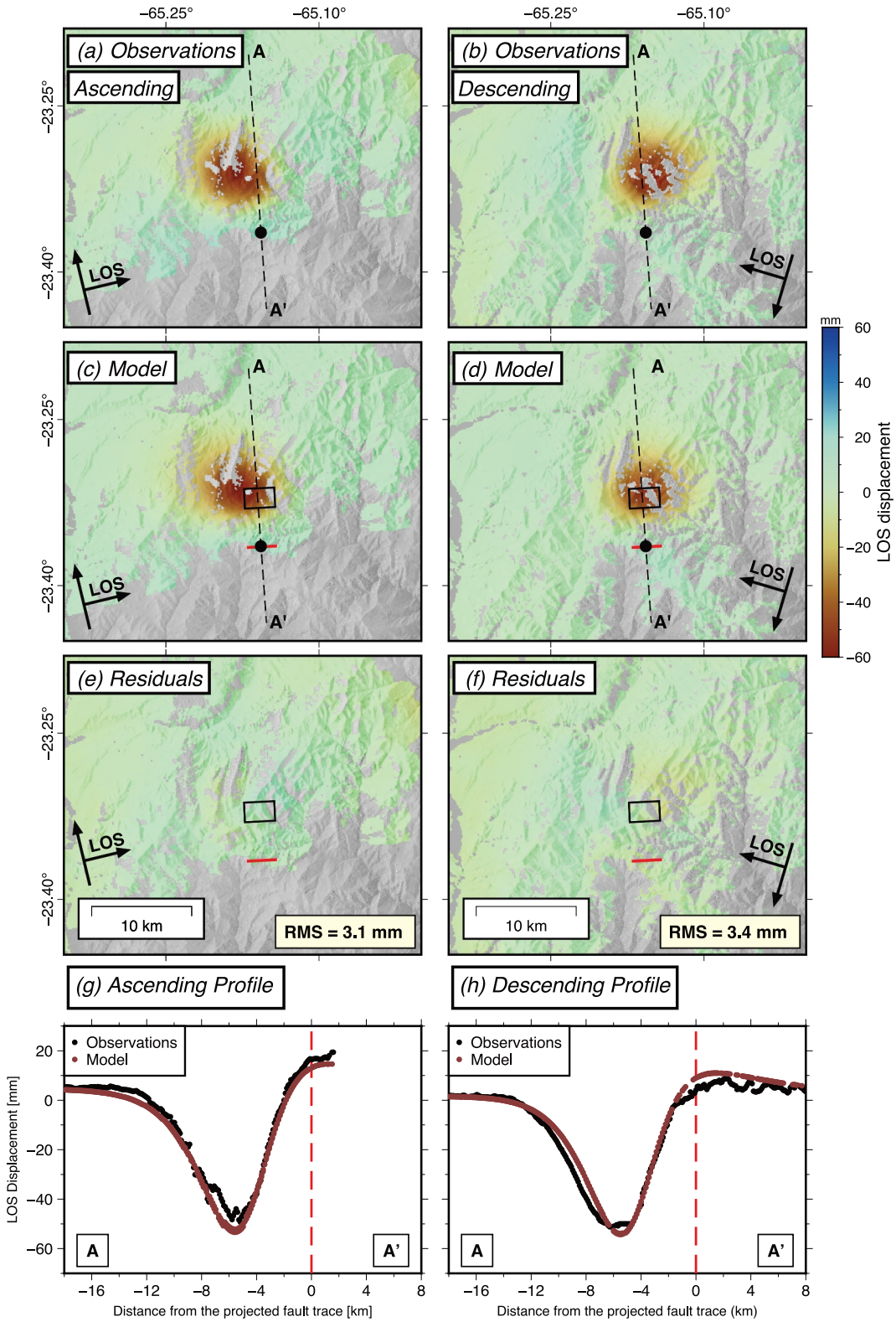

Figure 6. Results of the best-fitting uniform slip model for the 2020 Humahuaca earthquake. (a) and (b) show the observed, (c) and (d) modeled, and (e) and (f) residuals from our modeling of the coseismic displacements. The best-fit fault plane and the fault's surface projection are represented in (c–f) by the black box and red line, respectively. (g) and (h) compare profiles from A–A′ of the observed and modeled displacements for the ascending and descending tracks. The dashed vertical red line represents the position of the fault trace projected to the surface.

Our time-series reconstruction also reveals the spatio-temporal evolution of the postseismic deformation following the earthquake. We found postseismic LOS displacements of up to ∼2–3 cm located south of the peak in the coseismic displacement (Figures 5a and 5c and Figure S5 in Supporting Information S1 for descending observations). These signals were not resolvable in long temporal-baseline interferograms covering the same time period. A sensitivity analysis examining variations in the relaxation time parameter (τ) revealed minimal impact on the shape and amplitude of the reconstructed displacement fields (Figure 5b, and Figure S6 in Supporting Information S1), suggesting our observed postseismic displacements are robust.

3.3. Modeling of Coseismic and Postseismic Displacements

3.3.1. Geodetic Modeling Methods

We determined the best-fitting source parameters of the fault that ruptured in the 2020 Humahuaca earthquake by modeling the reconstructed coseismic displacement fields using a rectangular dislocation in an elastic half-space with uniform slip (Okada, 1985). The forward model parameters include the position and depth of the fault centroid, the fault length, width, strike, dip, rake, and the amount of slip. For computational efficiency, we downsampled the reconstructed coseismic LOS displacement (Figure S7 in Supporting Information S1) using an adaptive quadtree sampling method (Decriem et al., 2010). In order to determine the range of model parameters that fit the data, we used a Bayesian inversion scheme implemented in the software GBIS (Bagnardi & Hooper, 2018).

For moderate-magnitude earthquakes in which fault slip is buried at depth, like the Humahuaca event, the coseismic surface displacements are small and smooth, and it can be difficult to identify the fault plane using slip inversion methods (e.g., Biggs et al., 2006; Elliott et al., 2020; Lohman & Barnhart, 2010; Zhang et al., 2021). Therefore, we ran three separate inversions motivated by the E–W striking nodal planes of the focal mechanism derived from seismology (Figure S2 in Supporting Information S1). In the first inversion we constrained the fault plane to dip toward the north. In the second inversion we constrained the fault plane to dip toward the south. In the final inversion, the fault strike, dip and rake could take any value. Each model parameter was assigned an independent bounded uniform prior distribution within the limits listed in Table S3 in Supporting Information S1. The resulting best-fit solutions for these three inversions with the associated posterior probability density functions (PDFs) are shown in Figures S8 and S9 in Supporting Information S1, respectively.

To investigate the relationship between coseismic and postseismic slip, we extended the fault geometry constrained from the Bayesian inversion along its strike and dip directions by 10 km and subdivided the fault into 0.5 × 0.5 km patches. We then performed a non-negative least squares inversion for the distribution of slip on each fault patch that matches the pattern of the coseismic and postseismic deformation following the methodology of Funning, Parsons, et al. (2005). Within the inversion, we applied Laplacian smoothing to suppress unphysical oscillations in the slip distribution. We chose a smoothing factor of 150 based on an L-curve analysis, balancing solution roughness against model misfit (Figure S10 in Supporting Information S1). Implicit in our analysis is that the postseismic deformation is driven by afterslip around the margins of the coseismic rupture, which we consider justified given that the distribution of coseismic and postseismic surface displacement are similar. In addition, the seismogenic layer in the epicentral region is around 10–20 km thick (Cahill et al., 1992; Devlin et al., 2012), therefore it is likely that postseismic deformation is being accommodated by localized slip or shear on a fault or shear zone rather than by broadly distributed viscoelastic flow.

3.3.2. Uniform Slip Coseismic Fault Model

We found that uniform slip models were able to fit the data well for both north-dipping and south-dipping fault planes, with similar RMSE. There are no specific features in the InSAR data that can be used to distinguish between the two models. However, the RMSE for the north-dipping solution (3.3 mm) is marginally smaller than for a south-dipping plane (4.0 mm). The best-fitting model for a north-dipping fault plane has 1.04 m of slip on a 3.7 km wide by 3.0 km long normal fault (Figure 6). The strike of 266° is ∼E-W with a dip of 58° and a rake of −113°, indicative of normal faulting. The centroid depth is estimated at 5.8 km, and assuming a shear modulus of 30 GPa, the seismic moment is 3.46×10^{17} N m, corresponding to a moment magnitude of M_w 5.7.

The InSAR-derived source parameters are generally consistent with the seismological source parameters but with some key differences (Table 1). First, the location of the mid-point of the fault plane projected to the surface, as

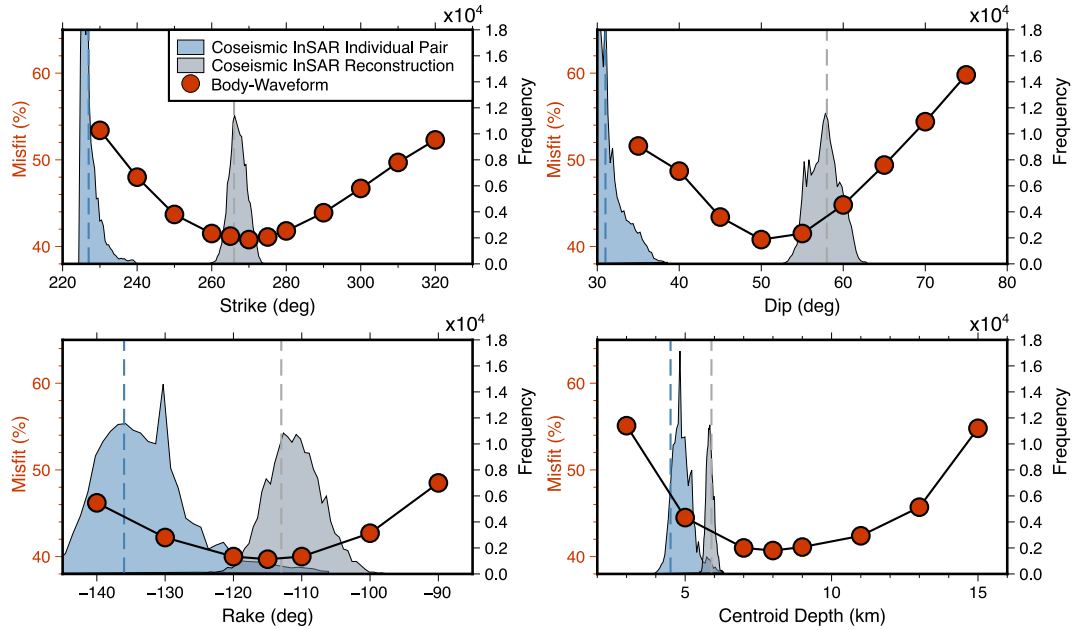

Figure 7. Sensitivity analysis of the fault source parameters from InSAR and body-waveform inversion. The vertical blue and gray dashed lines mark the optimal fault parameters determined from the individual coseismic displacements and the time-series reconstruction, respectively. The probability density functions of InSAR-derived source parameters are based on posterior distributions.

derived from InSAR modeling, differs from the centroid and epicentral locations reported in seismic catalogs by approximately 15–30 km (Figure 3). Specifically, the centroid and epicentral locations constrained by global seismic recordings (Global CMT, GEOFON, GEOSCOPE, and US Geological Survey) lie 15–18 km east of the InSAR-derived location. In contrast, the epicentral location reported by CSN, based on regional seismic recordings, lies about 30 km to the west of the InSAR-derived location. These discrepancies likely reflect differences in station density and location, which affect the accuracy of the locations reported in the earthquake catalogs. Second, the centroid depth for our preferred north-dipping solution is shallower compared to the centroid and hypocentral depth constraints from the seismic catalogs, with discrepancies ranging from ∼3 km relative to the GEOSCOPE hypocenter to ∼6 km relative to the Global CMT centroid. The body-waveform modeling yields a broad acceptable range for the north-dipping centroid depth of 5–13 km, whereas the InSAR inversion provides a narrower, best-fitting centroid depth range of 5.4–6.2 km.

We also performed additional inversions using the individual interferograms as the constraints to assess the extent to which our time-series reconstruction improves the constraints on the earthquake source parameters. We find that the posterior PDFs derived from inversions using the individual coseismic displacements deviate significantly from the independent estimates of the source parameters derived from body-waveform modeling (Figure 7). For example, the best-fit solution from individual coseismic displacement inversions for the north-dipping fault has discrepancies of 44° in strike, 20° in dip, and 21° in rake when compared to the body-waveform model. Additionally, the centroid depth is 3.5 km shallower. In contrast, the source model derived from the reconstructed coseismic displacement field is more consistent with the body-waveform modeling, with differences between best-fit solutions of ∼3° in strike, ∼7° in dip, and ∼1° in rake. This comparison suggests our time-series analysis methodology can significantly improve the accuracy of earthquake source parameters for buried moderate-magnitude events.

3.3.3. Distributed Slip Modeling of the Coseismic and Postseismic Displacements

The similarity between the pattern of the postseismic and coseismic deformation suggests the postseismic deformation likely reflects afterslip on the coseismic fault plane. To test this hypothesis, we solved for the distribution of both coseismic slip and afterslip needed to match the reconstructed coseismic and postseismic

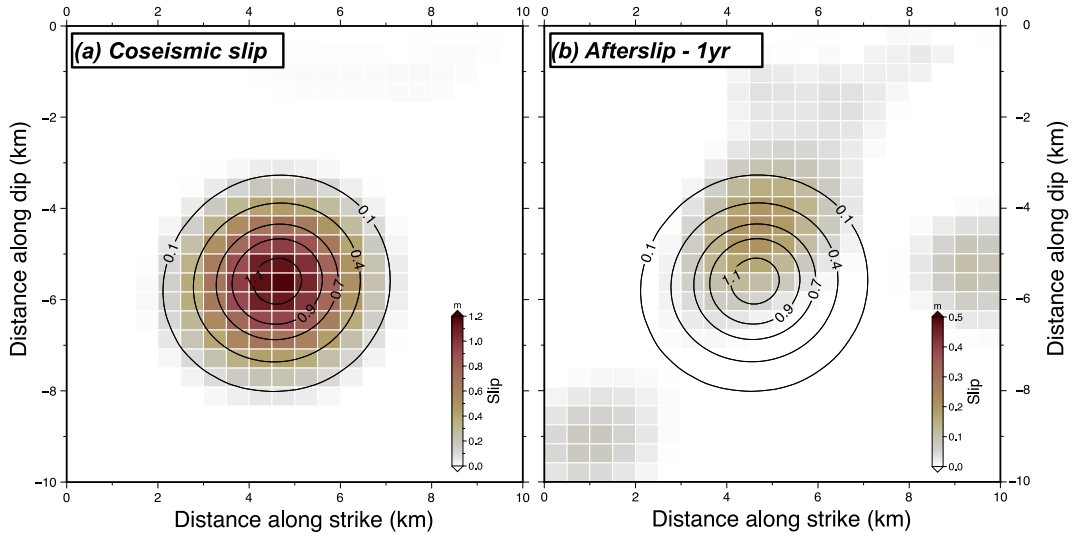

Figure 8. Preferred coseismic (a) and postseismic (b) slip distribution for the 2020 Humahuaca earthquake (north-dipping fault model). Contours show coseismic slip intervals in meters.

displacements using the methodology described in Section 3.3.1. Our preferred coseismic slip and afterslip models on a north-dipping fault plane are shown in Figure 8.

Our preferred model indicates that the postseismic afterslip occurred near the up-dip edge of the coseismic slip area (Figure 8b). A similar pattern has been observed following many normal-faulting earthquakes (Copley et al., 2012; D'Agostino et al., 2012; Ryder et al., 2010; Wimpenny et al., 2018; Yang et al., 2022). It is important to note that the afterslip patches observed at depths >8 km and near the lateral edges of the modeled fault plane (Figure 8b) are likely artifacts resulting from the limited resolution of the slip model (e.g., Biggs et al., 2006) and noise in the reconstructed postseismic displacement fields. The peak afterslip after 1 year reached 23 cm at a depth of 5 km, which is equivalent to ∼15% of the peak coseismic slip and a moment release of 17% of the coseismic moment. These values are consistent with proportions reported in previous studies of afterslip behavior across different tectonic settings, in which afterslip typically releases between 10% and 30% of the coseismic moment (Churchill et al., 2022).

We also tested the distribution of coseismic slip and afterslip for our south-dipping fault geometry (Figure S11 in Supportimg Information S1). This model placed afterslip in two distinct areas: one within the coseismic slip area at a depth of 4.5 km and another at the down-dip edge of the coseismic slip area at a depth of 9 km, with a peak slip of 25 cm. The occurrence of afterslip within the center of the coseismic slip zone is inconsistent with afterslip behavior, which typically occurs on the margins of the rupture area rather than within the rupture center (Avouac, 2015; Barbot et al., 2009; D'Agostino et al., 2012). All these findings further support the interpretation that the fault plane dips to the north.

3.4. Relationship Between Faulting and Pre-Existing Geological Structures

We find that the 2020 Humahuaca earthquake ruptured an ∼E–W trending, north-dipping normal fault and accommodated extension along an azimuth between 029° and 034°, therefore accommodating almost pure along-strike extension in the Andean Eastern Cordillera. Our modeling indicates that fault slip was confined between 3 and 8 km depth and that the fault's surface projection does not correlate with any pre-existing, geologically-mapped faults (Henriquez et al., 2022; Kley et al., 2005) (Figure 3c). The ∼NNE–SSW extensional kinematics of the earthquake contrast with the ∼E–W contractional kinematics of the major ∼NNE–SSW trending geological deformation structures in the region, suggesting there has been a change in the pattern of strain within the last ∼2 Ma from range-perpendicular shortening to present-day range-parallel extension.

4. Kinematic Implications of the 2020 Humahuaca Earthquake

In this section, we test three hypotheses for the cause of the range-parallel extension observed in Section 3 by combining our new source model for the 2020 Humahuaca earthquake with observations of thrust-earthquake slip vectors, GNSS horizontal velocities and topographic gradients.

4.1. Hypothetical Causes of Range-Parallel Extension

Figure 9 shows three possible kinematic models that could account for range-parallel extension in the Humahuaca region: divergent thrust-faulting on a curved range front (Figure 9a), strain partitioning due to oblique subduction (Figure 9b), or local shear caused by a transition in foreland shortening rates (Figure 9c). Below, we describe the kinematics and dynamical implications of each model. We then test them by analyzing the Humahuaca earthquake source parameters in the context of the GNSS velocity field and thrust earthquake slip vectors in the adjacent fold-thrust belt.

4.1.1. Divergent Thrust Faulting Model

In mountain belts with curved range fronts, the slip vectors of thrust-faulting earthquakes are often perpendicular to the range front (e.g., Molnar & Lyon-Caen, 1989; Nissen et al., 2011). This pattern of divergent thrust-faulting will lead to range-parallel extension within the mountain range that could be accommodated by normal faults (Figure 9a). The simplest dynamical interpretation of this pattern of deformation is that it reflects gravity-driven flow of the weak mountain crust over the rigid lowlands—a process often referred to as "gravitational spreading" (e.g., Copley & Mckenzie, 2007; England & McKenzie, 1982; Fleitout & Froidevaux, 1982; Flesch et al., 2001).

The divergent thrust-faulting model requires the range front to be curved and that the surface velocities and thrust-earthquake slip vectors are parallel to the direction of the maximum gradient in the local topography (Figure 9a). The model predicts that normal-faulting would accommodate extension perpendicular to the direction of thrust fault slip along the curved range front.

4.1.2. Strain Partitioning Model

Convergence between the Nazca and South American plates is rotated 15–16° anticlockwise relative to its trench-normal component due-west of Humahuaca (Jarrin et al., 2023). The combination of oblique convergence and mechanical locking on the subduction interface leads to right-lateral shearing of the Andes in a trench-parallel direction in the interseismic period between large subduction interface earthquakes (Bevis et al., 2001). In other similar settings, such shear is accommodated by trench-parallel strike-slip faulting (e.g., Marconato et al., 2024; Nocquet et al., 2014), block rotations within the overriding plate (e.g., Allmendinger et al., 2005; Beck, 1998), or a combination of both mechanisms (e.g., Jiang et al., 2022; La Femina et al., 2002). The strike-slip faults that accommodate trench-parallel motion may be locally transtensional in step-overs (Woodcock & Fischer, 1986), leading to normal-faulting earthquakes. This model of oblique convergence and strain partitioning is comparable to what has been proposed for certain parts of southern Tibet, where normal faulting is spatially associated with strike-slip faults (Murphy et al., 2014; Styron et al., 2011).

The strain partitioning model predicts an eastward decrease in range-parallel surface velocities from the Andes toward the foreland (Figure 9b). Notably, the surface velocities within the mountain range would not necessarily align with either the local topographic gradients or the slip vectors derived from thrust-faulting seismicity beneath the range front. The range front also does not have to be curved. The range-parallel shear can be taken up by faulting with different geometries, but we might expect to see evidence for right-lateral strike-slip faulting on range-parallel faults (Figure 9b), or clockwise block rotations in the central Andes (Beck, 1998).

4.1.3. Gradient in Shortening Rate Model

The 2020 Humahuaca earthquake occurred adjacent to an along-strike change from thin-to thick-skinned shortening on the Andes range front, which correlates with a north-to-south decrease in the total Neogene shortening (Kley et al., 1999) and therefore potentially a gradient in shortening rate. This north-to-south gradient in shortening could set up a zone of shear on E-W oriented planes (Figure 9c). There are multiple ways in which this deformation field may be accommodated, one of which is via conjugate strike-slip faults oriented approximately NE–SW and NW–SE along with normal faulting accommodating NE–SW extension (Figure 9c).

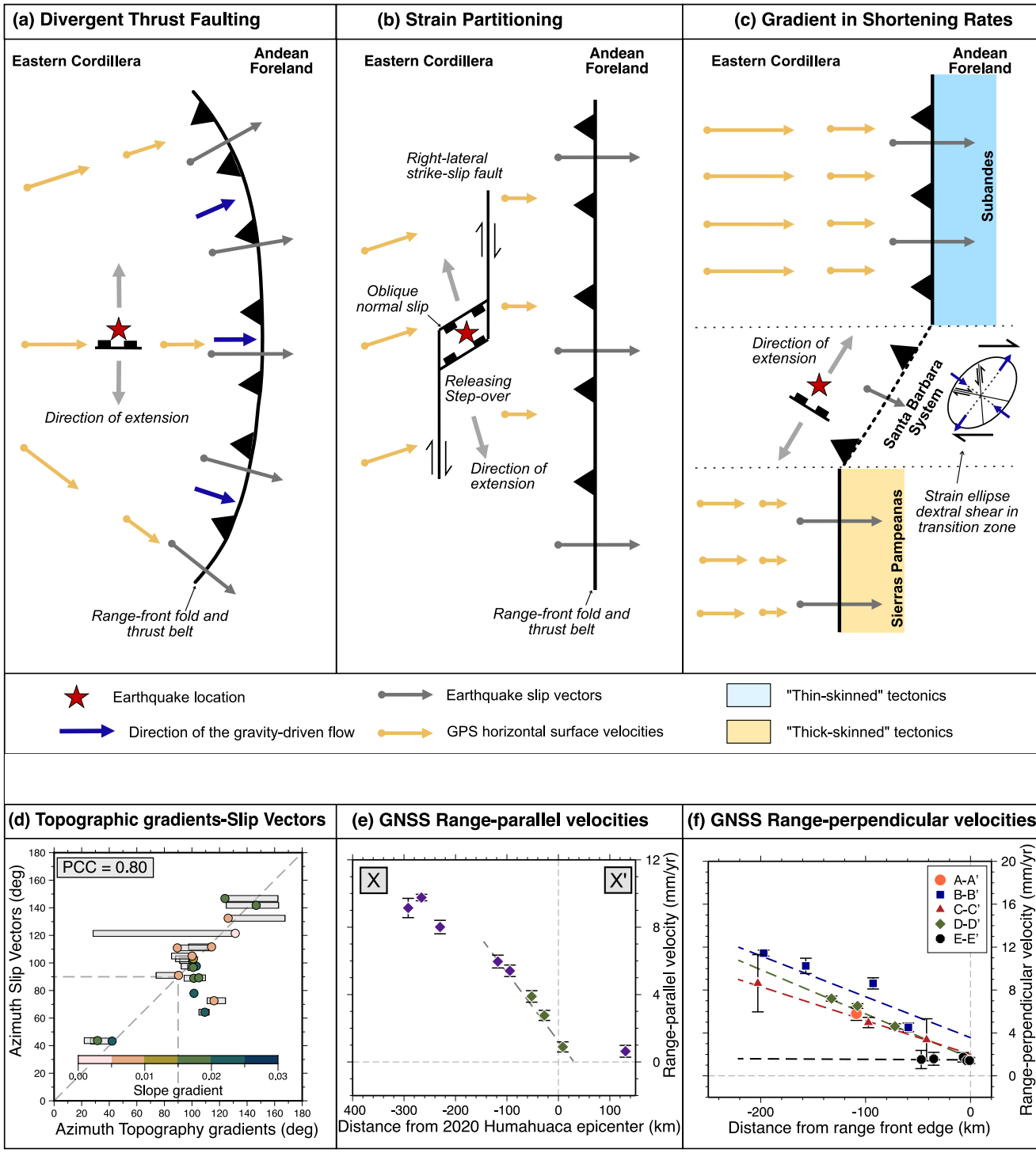

Figure 9. Three models that could account for range-parallel extension in the central Andes. (a) Divergent thrust-faulting along the range front, (b) oblique convergence between the Nazca Plate and South America that is partitioned within the overriding plate, and (c) a north-to-south decrease in the shortening rate leading to a zone of shear across E-W oriented planes and range-parallel stretching. Panels (d, e, and f) show the observations of earthquake slip vectors, topographic gradients and GNSS velocity fields in the central Andes. (d) Correlation between the azimuths of topographic gradients and slip vectors from 16°S–29°S, used to evaluate model (a). Light-gray bars indicate gradient azimuths for 100–300 km gaussian-filtered topography. Dot colors show slope steepness (0=low, 0.03=steep). PCC is Pearson Correlation Coefficient. (e) Range-parallel GNSS velocities along profile *X*–*X*′ in Figure 10d, used to evaluate model (b). (f) Range-perpendicular GNSS velocities along colored profiles in Figure 10d, used to evaluate model (c). Error bars in (e) and (f) are the 1σ velocity uncertainties. Dashed lines in (e) and (f) highlight velocity gradients discussed in the text.

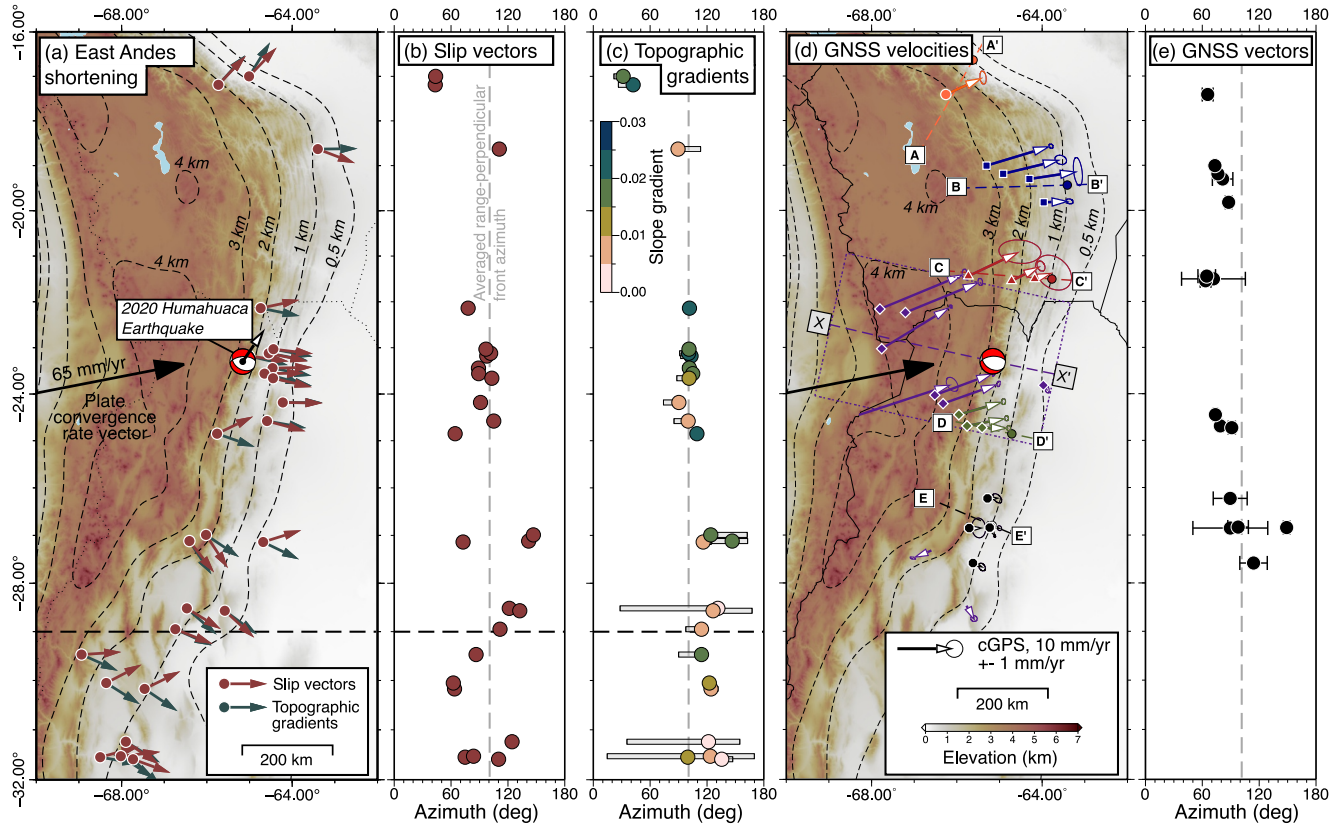

Figure 10. Relationship between thrust-earthquake slip vectors, topographic gradients, and GNSS horizontal velocities in the central Andes. (a) Well-constrained thrust-earthquake slip vectors (brown arrows) from Wimpenny and Watson (2020) and the azimuth of maximum topographic gradient (green arrows). The topographic gradients were calculated by applying a Gaussian filter with 300-km width to the SRTM 3-arc s elevation model (Farr et al., 2007). The filtered topography is shown by dashed black contours. The focal mechanism of the 2020 Humahuaca earthquake is shown in red along with the slip vector of the north-dipping fault plane constrained by InSAR. Panels (b) and (c) display the azimuths of the earthquake slip vectors and topographic gradients, respectively. Gray rectangles in (c) represent the range of azimuths derived using filter widths of 100, 200, and 300 km, with the circles showing the 300-km filter width. Dashed vertical gray lines in (b, c, and e) indicate the range-perpendicular azimuth averaged between latitudes 20°S and 26°S. (d) GNSS velocities compiled from McFarland et al. (2017), Figueroa et al. (2021) and Weiss et al. (2016) shown relative to stable South America with 1σ uncertainty ellipses. (e) Azimuths of GNSS velocity vectors along the mountain range. Error bars are the 1σ azimuth uncertainty. The black arrows in (a) and (d) represent the Nazca-South American plate convergence rate vector from Jarrin et al. (2023).

The shortening gradient model predicts a north-to-south decrease in the range-perpendicular GNSS velocities. Normal faulting could have a range of orientations, but instantaneous extension would be oblique to the plane of shear defined by the GNSS velocities.

4.2. Slip Vectors, Topographic Gradients and Range-Front Curvature

Figure 10 shows a comparison between the slip vector for the 2020 Humahuaca earthquake, the direction of maximum gradients in the long-wavelength topography, and slip vector azimuths from shallow moderate-magnitude (M_w 5.0–6.5) thrust-faulting earthquakes beneath the range front. Between 16°S and 29°S there is a strong positive correlation (Pearson correlation coefficient of 0.80; Figure 9d) between the azimuth of the maximum topographic gradient and thrust-earthquake slip vectors (Figures 10a–10c). South of 29°S, this correlation breaks down and the slip vectors are poorly correlated with topographic gradients. The kinematics of the range front are particularly well defined along the range front east of the 2020 Humahuaca earthquake—here a series of thrust-faulting earthquakes are accommodating shortening that is parallel to the topographic gradient and oblique to the Nazca-South America relative plate motion (Devlin et al., 2012; Wimpenny et al., 2018). The 2020 Humahuaca earthquake slip vector is almost perpendicular to these thrust-earthquake slip vectors. However, the range front topography between 18°S and 27°S is approximately linear (Figure 10c), and there is no resolvable divergence of the thrust-earthquake slip vectors (Figure 10b).

4.3. GNSS Velocity Field

Figure 10d shows a horizontal velocity field for the Andes back-arc created by combining GNSS velocities from McFarland et al. (2017), Figueroa et al. (2021) and Weiss et al. (2016). We only use velocities derived from continuously operating GNSS stations in the compilation to ensure the velocities are not affected by coseismic or postseismic deformation from megathrust earthquakes within the Nazca-South American subduction zone. All velocities were referenced relative to stable South America and we solved for a rotation for each independent data set that minimized the velocities of the GNSS stations in the foreland.

There are two main patterns in the GNSS velocity field. First, in the Puna plateau, the GNSS vectors have a similar azimuth to the Nazca-South America convergence vector, and they progressively rotate clockwise to become perpendicular to the range front toward the east (Figures 10d and 10e) (Bevis & Martel, 2001; McFarland et al., 2017; Weiss et al., 2016). As a result of this rotation, the correlation between GNSS vector azimuths and topographic gradients is moderate (Pearson correlation coefficient of 0.55; Figure S12 in Supporting Imformation S1). Figure 9e shows the range-parallel component of the velocity field projected onto the profile *X*–*X*' (Figure 10d), illustrating a linear decrease from 6 mm/yr to $\lesssim$1 mm/yr over a distance of ∼130 km, which is consistent with a range-parallel shear strain rate of ∼3–4 × 10^{-8} 1/yr. Second, the GNSS range-perpendicular velocities decrease in amplitude from west to east. Figure 9f shows the range-perpendicular velocities projected into a series of profiles across the range front shown in Figure 10d. We find that the shortening rates are highest in Bolivia (profile B-B′) but there is no resolvable decrease in the shortening rate between profiles *C*–*C*′ and *D*–*D*′ that span the section of range front with the 2020 Humahuaca earthquake.

4.4. Interpretation of the Kinematics

Our kinematic analyses allow us to test the hypotheses presented in Section 4.1. The clearest observation is that the GNSS velocity field is not consistent with the hypothesis that a north-to-south gradient in shortening rate across the Andean foreland near Humahuaca leads to localized range-parallel extension (Figures 9c and 9f). The data are, however, mostly consistent with our two other hypotheses.

Thrust-earthquake slip vectors and GNSS velocity azimuths along the range front are sub-parallel to topographic gradients, implying gravity-driven flow is controlling the azimuth of thrust-faulting around the eastern margin of the Andes. GNSS velocity azimuths within the high mountains, however, are oblique to the topographic gradients and the adjacent range front. Nevertheless, because the Andes range front is approximately linear between 19°S and 27°S, there is little measurable divergence in the thrust-earthquake slip vectors or GNSS velocities within their uncertainties (Figures 10d and 10e). A similar configuration is observed in the maximum horizontal compression (SHmax) orientations to the north and south of the Humahuaca event, where little variation along the strike of the range front has been measured (Assumpção et al., 2016; Fernández et al., 2024). As a result, there will be slow, if any, range-parallel extensional strain near Humahuaca caused by divergent thrust-faulting.

The characteristics of the velocity field in the eastern Andes are consistent with numerical models of gravitational spreading of a fluid mountain range that impose an oblique, plate-convergence–like push behind a straight range front (Knight, 2023). The linear range front and lack of velocity divergence may represent an early stage in the evolution of mountain-front curvature (Copley, 2012). Furthermore, theoretical models of gravity-driven flow of a mountain range over a rigid foreland indicate that the timescale needed to develop constant curvature across the range front from an initially linear mountain range (Equation 3 in Copley (2012)) is on the order of 9–90 Myrs in the case of the eastern Andes (using average crustal viscosity estimated at $\sim 10^{21} - 10^{22}$ Pa s for the central Andes by Lamb (2000); Husson and Ricard (2004)). These timescales suggest that the present day curvature is unlikely to have developed within the last 2 Myr, the period during which extension in the Humahuaca region may have begun. However, the assumption of an initially linear mountain range in the Andes is likely to be incorrect, given the well-established effects of foreland rheology on controlling the distribution of active deformation (Kley & Monaldi, 1998; Watts et al., 1995).

The strain partitioning hypothesis is also consistent with our observations. The GNSS vectors rotate clockwise from within the Puna plateau toward the Andean foreland, indicating there is ∼3–4 × 10^{-8} 1/yr of range-parallel shear. We do not observe any steps in range-parallel velocities associated with strain accumulation around individual strike-slip faults within the Eastern Cordillera (Figueroa et al., 2021; McFarland et al., 2017). Two possibilities are that the velocity field is accommodated by a series of sub-parallel ∼NNE-SSW trending right-

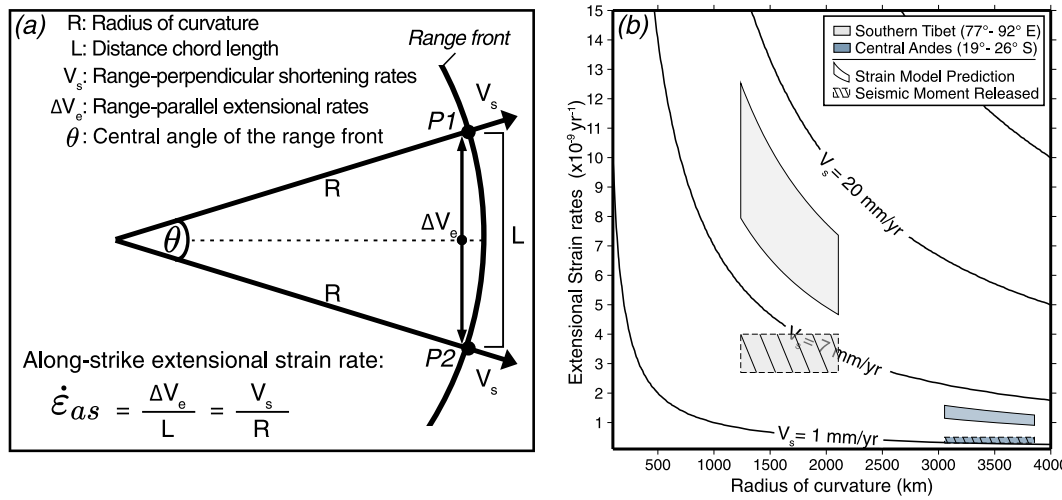

Figure 11. Predicted range-parallel extensional strain rate from a simple divergent thrust-faulting model. (a) Conceptual model linking range-perpendicular shortening rates and the curvature of the range front to the range-parallel extensional strain rate. (b) Predicted and observed range-parallel extensional strain rates as a function of radius of curvature for southern Tibet and central Andes based on the setup in (a). Filled polygons represent predicted extensional strain rates using shortening rates determined by GNSS (Styron et al., 2011). Dashed polygons show strain rates derived from a moment-tensor summation of normal-faulting earthquakes (Figure S13 in Supporting Information S1) using the method of Kostrov (1974). Moment-tensor summation of all the earthquakes in each region is shown in Table S2 in Supporting Information S1. Contours indicate range-perpendicular shortening rates (V_s).

lateral strike-slip faults (Funning, Barke, et al., 2005), or that it is accommodated by clockwise rotations about vertical axes of blocks bounded by strike-slip faults oblique to the range front (McFarland et al., 2017). Further observations of the geometry of active strike-slip faults accommodating the velocity field are needed to differentiate between these options.

5. Discussion

5.1. Comparison of the Central Andes With Southern Tibet

The primary distinction between range-parallel extension in the central Andes and southern Tibet lies in the rate, distribution and cumulative slip of the normal faulting. In southern Tibet, range-parallel extension affects a region spanning over 1,000 km of the Himalaya at a rate of ~30 mm/yr (Styron et al., 2011) and is associated with major intra-montane basins bound by faults with kilometers of cumulative slip (Armijo et al., 1986) and frequent moderate-magnitude seismicity (Elliott et al., 2010). In contrast, in the central Andes, evidence of range-parallel extension is primarily provided by the 2020 Humahuaca earthquake, range-perpendicular normal fault grabens are absent from the geomorphology, and the along-strike extension is below the resolution of the existing GNSS velocity measurements. The natural question is whether these differences can be explained by the same root cause of range-parallel extension.

If divergent thrust-faulting is the cause of the range-parallel extension in both settings and thrust-fault slip vectors are perpendicular to the range front, then the differences in the along-strike extensional strain rate $\dot{\varepsilon}_{as}$ should simply be a result of differences in the rate of range front shortening V_s and the radius of curvature of the range front R through the relationship: $\dot{\varepsilon}_{as} = V_s/R$ (Figure 11a, derivation presented in Text S1 in Supporting Information S1).

For southern Tibet, the predicted range-parallel strain rate using our simple model is 5–12 × 10^{-9} 1/yr (Figure 11b), which is consistent with the geological estimates of 3–10 × 10^{-9} 1/yr from slip-rate measurements across normal-fault grabens (Armijo et al., 1986) and geodetic estimates of 5–30 × 10^{-9} 1/yr derived from GNSS measurements (Styron et al., 2011; Zheng et al., 2017). We estimate the range-parallel strain rate from summing normal-faulting earthquake moment tensors to be 2–4 × 10^{-9} 1/yr, which is 10%–50% of the predicted rate (e.g., Elliott et al., 2010). For the section of the Andes between 19° S and 26° S that spans the 2020 Humahuaca

earthquake epicenter, the predicted range-parallel extensional strain rate is 1–2 × 10^{-9} 1/yr (Figure 11b), as the radius of curvature is ∼2-times larger and the shortening rate ∼3-times slower than in southern Tibet. As the 2020 Humahuaca earthquake is the only normal-faulting earthquake in the central Andes in the last 50 years, we calculate maximum strain rate of 0.2–0.5 × 10^{-9} 1/yr. As in southern Tibet, this suggests that 15%–50% of the range-parallel strain rate is accounted for by earthquakes. From this analysis, the more frequent normal-faulting seismicity in southern Tibet can be explained simply by the more curved mountain range front and the faster shortening rate compared to the central Andes. Given that the onset of range-parallel extension at Humahuaca could be as recent as ∼2 Ma, whereas extension in Tibet initiated ∼10–15 Ma (e.g., Armijo et al., 1986; Styron et al., 2011), then the normal faults in the central Andes have accumulated far less slip than those in southern Tibet. This can explain why there is no geomorphological expression of range-parallel faulting in the central Andes.

A similar geometrical model does not exist for the strain partitioning model where extension is occurring within transtensional step-overs (Figure 9b). However, with this model we expect that for higher rates of range-parallel shear there should be higher rates of range-parallel extension. For southern Tibet, Styron et al. (2011) find range-parallel shear rates between 3 and 8 mm/yr across a distance of ∼200–300 km, equivalent to a range-parallel shear strain rate of 1–4 × 10^{-8} 1/yr. This estimate is similar to, or even less than, the range-parallel shear strain rates across the central Andes (3–4 × 10^{-8} 1/yr). Therefore, the significant differences in the rates of range-parallel extension between southern Tibet and the central Andes cannot be explained solely by strain partitioning.

5.2. Implications for Seismic Hazard

Existing probabilistic seismic hazard analyses (PSHAs) for South America simulate earthquake sources using smoothed seismicity grids and known crustal faults (Johnson et al., 2023; Petersen et al., 2018). Although, to our knowledge, the 2020 Humahuaca earthquake is the first instrumentally recorded normal-faulting earthquake in the Eastern Cordillera and ruptured a previously unmapped fault, both the divergent thrust-faulting and strain partitioning models indicate that future normal-faulting earthquakes similar to Humahuaca may occur elsewhere in the Eastern Cordillera. Therefore, the existing PSHAs could underestimate the seismic hazard in this region of the central Andes where population density is significant (Figure S14 in Supporting Information S1).

The divergent thrust-faulting model forecasts a moment release rate of 2.6–4.7 × 10^{16} Nm/yr in the Eastern Cordillera, equivalent to one M_w 6.0–6.2 normal-faulting earthquake every 50 years if we assume a seismogenic thickness of 15 km and a rigidity modulus of 32 GPa. Forecasts of moment release due to normal faulting from the strain partitioning model are dependent on the number of step-overs in the fault system accommodating range-parallel shear, which remains poorly understood.

5.3. Time-Series Reconstruction for M5–6 Earthquakes

Previous InSAR analyses of the 2020 Humahuaca earthquake identified up to ∼7 cm of negative LOS displacement using an ascending Sentinel-1 pair (25 Nov–01 Dec 2020) and up to ∼9 cm in a 2-year SAOCOM-1 interferogram (01 May 2020–09 Jul 2021) (Delgado et al., 2024). However, no deformation signal was clearly detected above the background noise levels in the Sentinel-1 descending track (Delgado et al., 2024). Furthermore, semi-automated inversions based on individual interferograms suggested predominantly oblique-slip solutions (Shea & Barnhart, 2022) whose rakes and strikes differ by 20–50° and 12–21°, respectively, from our time-series reconstruction (Table 1). These contrasts illustrate how atmospheric noise in individual interferograms can affect fault geometry estimates and, therefore, interpretations of the direction of the extension in the central Andes.

Our time-series reconstruction also captured ∼3 cm of transient postseismic LOS displacement in the 2 years following the earthquake. Modeling these signals as afterslip helps discriminate between alternative dip directions of the buried fault plane (Section 3.3). In summary, multi-parameter InSAR time-series analysis both lowers noise and captures the spatio-temporal evolution of coseismic and postseismic deformation when displacement follows a simple functional form (D'Agostino et al., 2012; Zhou et al., 2018).

6. Conclusions

The 2020 M_w 5.7 Humahuaca earthquake provides clear evidence of active range-parallel extension in the central Andes. Using observations from Sentinel-1 InSAR time-series and body-waveform seismology, we find the Humahuaca earthquake ruptured a 6 km deep, buried, north-dipping normal fault that cross-cuts pre-existing geological structures related to Neogene shortening in the Eastern Cordillera. The earthquake accommodated NNE–SSW extension, which is parallel to the Andean range front and has similar kinematics to the more well-known examples of range-parallel extension in southern Tibet. By combining our source model for the Humahuaca earthquake with regional GNSS and earthquake slip vector measurements, we propose that range-parallel extension could be a result of either divergent thrust-faulting or strain partitioning within the Eastern Cordillera. An important unanswered question is how the range-parallel shear observed in the GNSS velocity field across the eastern Andes is accommodated by active faulting. Further geomorphological mapping of Quaternary faulting and a denser GNSS network between latitudes 23°S and 25°S across the Puna and Eastern Cordillera could address this question and reduce uncertainty in the potential seismic sources in the eastern Andes.

Conflict of Interest

The authors declare no conflicts of interest relevant to this study.

Data Availability Statement

All interferograms can be accessed through the COMET-LiCSAR portal (https://comet.nerc.ac.uk/comet-lics-portal/) and the CEDA archive (https://data.ceda.ac.uk/neodc/comet/data/licsar_products). All seismic data were downloaded through the EarthScope Consortium Wilber 3 system (http://ds.iris.edu/wilber3/). The GNSS velocities are compiled from published studies: Weiss et al. (2016), McFarland et al. (2017), and Figueroa et al. (2021). The uniform slip modeling was carried out on GBIS software (https://comet.nerc.ac.uk/gbis/). All of the codes and data needed to reproduce the InSAR time-series reconstruction and InSAR-derived modeling in GBIS are available from https://doi.org/10.5281/zenodo.15658649 (Orrego et al., 2025).

Acknowledgments

SO was supported by the National Agency for Research and Development (ANID)/ DOCTORADO BECAS CHILE/ 72220148, and SO, SW, JB, and YM were supported by the NERC Centre for the Observation and Modelling of Earthquakes, Volcanoes and Tectonics (COMET) a partnership between UK Universities and the British Geological Survey. JB was supported by the European Research Council (ERC) under the European Union's Horizon 2020 research and innovation programme (MAST; Grant agreement No. 101003173). SW was supported by a Start Up Grant from the University of Bristol. The InSAR and time-series processing of this work was undertaken on JASMIN, the UK's collaborative data analysis environment (https://www.jasmin.ac.uk). Figures were drafted using the free software PyGMT: A Python interface for the Generic Mapping Tools, version 0.13.0 (Tian et al., 2024) and Generic Mapping Tools, version 6.5 (Wessel et al., 2019). We also thank the Editor, Anke Friedrich, the Associate Editor, one anonymous reviewer and Marcelo Assumpção for their constructive reviews.

References

Allmendinger, R. W., Smalley, R., Bevis, M., Caprio, H., & Brooks, B. (2005). Bending the Bolivian orocline in real time. *Geology*, *33*(11), 905–908. https://doi.org/10.1130/G21779.1

Allmendinger, R. W., Strecker, M., Eremchuk, J. E., & Francis, P. (1989). Neotectonic deformation of the southern Puna Plateau, northwestern Argentina. *Journal of South American Earth Sciences*, *2*(2), 111–130. https://doi.org/10.1016/0895-9811(89)90040-0

Alvarado, P., & Beck, S. (2006). Source characterization of the San Juan (Argentina) crustal earthquakes of 15 January 1944 (Mw 7.0) and 11 June 1952 (Mw 6.8). *Earth and Planetary Science Letters*, *243*(3–4), 615–631. https://doi.org/10.1016/J.EPSL.2006.01.015

Armijo, R., Tapponnier, P., Mercier, J. L., & Han, T.-L. (1986). Quaternary extension in southern Tibet: Field observations and tectonic implications. *Journal of Geophysical Research*, *91*(B14), 13803–13872. https://doi.org/10.1029/JB091IB14P13803

Assumpção, M., & Araujo, M. (1993). Effect of the Altiplano-Puna plateau, South America, on the regional intraplate stresses. *Tectonophysics*, *221*(3–4), 475–496. https://doi.org/10.1016/0040-1951(93)90174-I

Assumpção, M., Dias, F. L., Zevallos, I., & Naliboff, J. B. (2016). Intraplate stress field in South America from earthquake focal mechanisms. *Journal of South American Earth Sciences*, *71*, 278–295. https://doi.org/10.1016/J.JSAMES.2016.07.005

Avouac, J. P. (2015). From geodetic imaging of seismic and aseismic fault slip to dynamic modeling of the seismic cycle. *Annual Review of Earth and Planetary Sciences*, *43*(1), 233–271. https://doi.org/10.1146/annurev-earth-060614-105302

Bagnardi, M., & Hooper, A. (2018). Inversion of surface deformation data for rapid estimates of source parameters and uncertainties: A Bayesian approach. *Geochemistry, Geophysics, Geosystems*, *19*(7), 2194–2211. https://doi.org/10.1029/2018GC007585

Barbot, S., Fialko, Y., & Bock, Y. (2009). Postseismic deformation due to the Mw 6.0 2004 Parkfield earthquake: Stress-driven creep on a fault with spatially variable rate-and-state friction parameters. *Journal of Geophysical Research*, *114*(B7), 7405. https://doi.org/10.1029/2008JB005748

Barrientos, S., & Team, N. S. C. C. (2018). The seismic network of Chile. *Seismological Research Letters*, *89*(2A), 467–474. https://doi.org/10.1785/0220160195

Beck, M. E. (1998). On the mechanism of crustal block rotations in the central Andes. *Tectonophysics*, *299*(1–3), 75–92. https://doi.org/10.1016/S0040-1951(98)00199-1

Bevis, M., Kendrick, E., Smalley, R., Brooks, B., Allmendinger, R., & Isacks, B. (2001). On the strength of interplate coupling and the rate of back arc convergence in the central Andes: An analysis of the interseismic velocity field. *Geochemistry, Geophysics, Geosystems*, *2*(11). https://doi.org/10.1029/2001gc000198

Bevis, M., & Martel, S. J. (2001). Oblique plate convergence and interseismic strain accumulation. *Geochemistry, Geophysics, Geosystems*, *2*(8). https://doi.org/10.1029/2000GC000125

Biggs, J., Bergman, E., Emmerson, B., Funning, G. J., Jackson, J., Parsons, B., & Wright, T. J. (2006). Fault identification for buried strike-slip earthquakes using InSAR: The 1994 and 2004 Al Hoceima, Morocco earthquakes. *Geophysical Journal International*, *166*(3), 1347–1362. https://doi.org/10.1111/j.1365-246X.2006.03071.x

Blom, N., Hardalupas, P. S., & Rawlinson, N. (2022). Mitigating the effect of errors in source parameters on seismic (waveform) tomography. *Geophysical Journal International*, *232*(2), 810–828. https://doi.org/10.1093/GJI/GGAC314

Cabrera, J., & Sébrier, M. (1998). Surface rupture associated with a 5.3-mb earthquake: The 5 April 1986 Cuzco earthquake and kinematics of the Chincheros-Quoricocha faults of the High Andes, Peru. *Bulletin of the Seismological Society of America*, *88*(1), 242–255. https://doi.org/10.1785/BSSA0880010242

Cahill, T., Isacks, B. L., Whitman, D., Chatelain, J.-L. C., Perez, A., & Chiu, J. M. (1992). Seismicity and tectonics in Jujuy Province, northwestern Argentina. *Tectonics*, *11*(5), 944–959. https://doi.org/10.1029/92TC00215

Churchill, R. M., Werner, M. J., & Biggs, J., & Fagereng, B. A. (2022). Afterslip moment scaling and variability from a global compilation of estimates. *Journal of Geophysical Research: Solid Earth*, *127*(4), e2021JB023897. https://doi.org/10.1029/2021JB023897

Coira, B., Davidson, J., Mpodozis, C., & Ramos, V. (1982). Tectonic and magmatic evolution of the Andes of northern Argentina and Chile. *Earth-Science Reviews*, *18*(3–4), 303–332. https://doi.org/10.1016/0012-8252(82)90042-3

Cook, K. L., & Royden, L. H. (2008). The role of crustal strength variations in shaping orogenic plateaus, with application to Tibet. *Journal of Geophysical Research*, *113*(8). https://doi.org/10.1029/2007JB005457

Copley, A. (2012). The formation of mountain range curvature by gravitational spreading. *Earth and Planetary Science Letters*, *351–352*, 208–214. https://doi.org/10.1016/j.epsl.2012.07.036

Copley, A., Avouac, J. P., & Wernicke, B. P. (2011). Evidence for mechanical coupling and strong Indian lower crust beneath southern Tibet. *Nature*, *472*(7341), 79–81. https://doi.org/10.1038/nature09926

Copley, A., Boait, F., Hollingsworth, J., Jackson, J., & McKenzie, D. (2009). Subparallel thrust and normal faulting in Albania and the roles of gravitational potential energy and rheology contrasts in mountain belts. *Journal of Geophysical Research*, *114*(5). https://doi.org/10.1029/2008JB005931

Copley, A., Hollingsworth, J., & Bergman, E. (2012). Constraints on fault and lithosphere rheology from the coseismic slip and postseismic afterslip of the 2006 Mw7.0 Mozambique earthquake. *Journal of Geophysical Research*, *117*(B3), 3404. https://doi.org/10.1029/2011JB008580

Copley, A., & Mckenzie, D. (2007). Models of crustal flow in the India-Asia collision zone. *Geophysical Journal International*, *169*(2), 683–698. https://doi.org/10.1111/j.1365-246X.2007.03343.x

Craig, T. J., Jackson, J., Priestley, K., & Ekström, G. (2023). A cautionary tale: Examples of the mis-location of small earthquakes beneath the Tibetan plateau by routine approaches. *Geophysical Journal International*, *233*(3), 2021–2038. https://doi.org/10.1093/GJI/GGAD025

D'Agostino, N., Cheloni, D., Fornaro, G., Giuliani, R., & Reale, D. (2012). Space-time distribution of afterslip following the 2009 L'Aquila earthquake. *Journal of Geophysical Research*, *117*(B2), 2402. https://doi.org/10.1029/2011JB008523

Dalmayrac, B., & Molnar, P. (1981). Parallel thrust and normal faulting in Peru and constraints on the state of stress. *Earth and Planetary Science Letters*, *55*(3), 473–481. https://doi.org/10.1016/0012-821X(81)90174-6

Daout, S., Steinberg, A., Isken, M. P., Heimann, S., & Sudhaus, H. (2020). Illuminating the spatio-temporal evolution of the 2008–2009 Qaidam earthquake sequence with the joint use of Insar time series and teleseismic data. *Remote Sensing*, *12*(17), 1–23. https://doi.org/10.3390/rs12172850

Daout, S., Sudhaus, H., Kausch, T., Steinberg, A., & Dini, B. (2019). Interseismic and postseismic shallow creep of the North Qaidam thrust faults detected with a multitemporal InSAR analysis. *Journal of Geophysical Research: Solid Earth*, *124*(7), 7259–7279. https://doi.org/10.1029/2019JB017692

Daxberger, H., & Riller, U. (2015). Kinematics of neogene to recent upper-crustal deformation in the southern Central Andes (23°–28°C) inferred from fault–slip analysis: Evidence for gravitational spreading of the Puna Plateau. *Tectonophysics*, *642*(1), 16–28. https://doi.org/10.1016/J.TECTO.2014.12.003

Decriem, J., Árnadóttir, T., Hooper, A., Geirsson, H., Sigmundsson, F., Keiding, M., et al. (2010). The 2008 May 29 earthquake doublet in SW Iceland. *Geophysical Journal International*, *181*(2), 1128–1146. https://doi.org/10.1111/J.1365-246X.2010.04565.X

Delgado, F., Shreve, T., Borgstrom, S., Leon-Ibanez, P., Castillo, J. D., & Poland, M. (2024). A global assessment of SAOCOM-1 L-band stripmap data for InSAR characterization of volcanic, tectonic, cryospheric, and anthropogenic deformation. *IEEE Transactions on Geoscience and Remote Sensing*, *62*, 1–21. https://doi.org/10.1109/TGRS.2024.3423792

Devlin, S., Isacks, B. L., Pritchard, M. E., Barnhart, W. D., & Lohman, R. B. (2012). Depths and focal mechanisms of crustal earthquakes in the central Andes determined from teleseismic waveform analysis and InSAR. *Tectonics*, *31*(2). https://doi.org/10.1029/2011TC002914

Doin, M.-P., Lodge, F., Guillaso, S., Jolivet, R., Lasserre, C., Ducret, G., et al. (2011). Presentation of the Small Baseline NSBAS processing chain on a case example: The Etna deformation monitoring from 2003 to 2010 using ENVISAT data. Proceedings of the Fringe symposium, 1–7.

Ekström, G., Nettles, M., & Dziewoński, A. M. (2012). The global CMT project 2004-2010: Centroid-moment tensors for 13,017 earthquakes. *Physics of the Earth and Planetary Interiors*, *200–201*, 1–9. https://doi.org/10.1016/j.pepi.2012.04.002

Elliott, J. R., de Michele, M., & Gupta, H. K. (2020). Earth observation for crustal tectonics and earthquake hazards. *Surveys in Geophysics*, *41*(6), 1355–1389. https://doi.org/10.1007/s10712-020-09608-2

Elliott, J. R., Walters, R. J., England, P. C., Jackson, J. A., Li, Z., & Parsons, B. (2010). Extension on the Tibetan plateau: Recent normal faulting measured by InSAR and body wave seismology. *Geophysical Journal International*, *183*(2), 503–535. https://doi.org/10.1111/J.1365-246X.2010.04754.X

England, P., & Houseman, G. (1989). Extension during continental convergence, with application to the Tibetan Plateau. *Journal of Geophysical Research*, *94*(B12), 17561–17579. https://doi.org/10.1029/JB094IB12P17561

England, P., & McKenzie, D. (1982). A thin viscous sheet model for continental deformation. *Geophysical Journal International*, *70*(2), 295–321. https://doi.org/10.1111/J.1365-246X.1982.TB04969.X

England, P. C., & Houseman, G. A. (1988). The mechanics of the Tibetan Plateau. *Philosophical Transactions of the Royal Society of London. Series A, Mathematical and Physical Sciences*, *326*(1589), 301–320. https://doi.org/10.1098/RSTA.1988.0089

Farr, T. G., Rosen, P. A., Caro, E., Crippen, R., Duren, R., Hensley, S., et al. (2007). The shuttle radar topography mission. *Reviews of Geophysics*, *45*(2). https://doi.org/10.1029/2005RG000183

Fernández, M. G. A., Assumpção, M., Cesca, S., & Nieto, M. (2024). Crustal seismicity and updated stress mapping in the Bolivian Orocline, Central Andes. *Journal of South American Earth Sciences*, *149*, 105187. https://doi.org/10.1016/J.JSAMES.2024.105187

Ferreira, A. M., Weston, J., & Funning, G. J. (2011). Global compilation of interferometric synthetic aperture radar earthquake source models: 2. Effects of 3-D Earth structure. *Journal of Geophysical Research*, *116*(B8), B08409. https://doi.org/10.1029/2010JB008132

Figueroa, S., Weiss, J. R., Hongn, F., Pingel, H., Escalante, L., Elías, L., et al. (2021). Late Pleistocene to recent deformation in the thick-skinned fold-and-thrust belt of northwestern Argentina (Central Calchaquí Valley, 26°S). *Tectonics*, *40*(1), e2020TC006394. https://doi.org/10.1029/2020TC006394

Fleitout, L., & Froidevaux, C. (1982). Tectonics and topography for a lithosphere containing density heterogeneities. *Tectonics*, *1*(1), 21–56. https://doi.org/10.1029/TC001I001P00021

Flesch, L. M., Haines, A. J., & Holt, W. E. (2001). Dynamics of the India-Eurasia collision zone. *Journal of Geophysical Research*, *106*(B8), 16435–16460. https://doi.org/10.1029/2001JB000208

Funning, G. J., Barke, R. M., Lamb, S. H., Minaya, E., Parsons, B., & Wright, T. J. (2005). The 1998 Aiquile, Bolivia earthquake: A seismically active fault revealed with InSAR. *Earth and Planetary Science Letters*, *232*(1–2), 39–49. https://doi.org/10.1016/J.EPSL.2005.01.013

Funning, G. J., Parsons, B., Wright, T. J., Jackson, J. A., & Fielding, E. J. (2005). Surface displacements and source parameters of the 2003 Bam (Iran) earthquake from Envisat advanced synthetic aperture radar imagery. *Journal of Geophysical Research*, *110*(9), 1–23. https://doi.org/10.1029/2004JB003338

Gao, Y., Tilmann, F., van Herwaarden, D. P., Thrastarson, S., Fichtner, A., Heit, B., et al. (2021). Full waveform inversion beneath the Central Andes: Insight into the dehydration of the Nazca Slab and delamination of the back-arc lithosphere. *Journal of Geophysical Research: Solid Earth*, *126*(7), e2021JB021984. https://doi.org/10.1029/2021JB021984

Garth, T., Sigloch, K., & Storchak, D. (2023). ISC-PPSM: Assessing moment tensor resolution, and addressing shallow earthquake depth resolution. XXVIII General Assembly of the International Union of Geodesy and Geophysics (IUGG). https://doi.org/10.57757/IUGG23-2916

Goldstein, R. M., & Werner, C. L. (1998). Radar interferogram filtering for geophysical applications. *Geophysical Research Letters*, *25*(21), 4035–4038. https://doi.org/10.1029/1998GL900033

Guns, K., Xu, X., Bock, Y., & Sandwell, D. (2022). GNSS-corrected InSAR displacement time-series spanning the 2019 Ridgecrest, CA earthquakes. *Geophysical Journal International*, *230*(2), 1358–1373. https://doi.org/10.1093/gji/ggac121

Henriquez, S., DeCelles, P. G., Carrapa, B., & Hughes, A. N. (2022). Kinematic evolution of the central Andean retroarc thrust belt in northwestern Argentina and implications for coupling between shortening and crustal thickening. *Bulletin of the Geological Society of America*, *135*(1–2), 81–103. https://doi.org/10.1130/B36231.1

Horton, B. K. (2018). Sedimentary record of Andean mountain building. *Earth-Science Reviews*, *178*, 279–309. https://doi.org/10.1016/j.earscirev.2017.11.025

Husson, L., & Ricard, Y. (2004). Stress balance above subduction: Application to the Andes. *Earth and Planetary Science Letters*, *222*(3–4), 1037–1050. https://doi.org/10.1016/J.EPSL.2004.03.041

Jarrin, P., Nocquet, J. M., Rolandone, F., Mora-Páez, H., Mothes, P., & Cisneros, D. (2023). Current motion and deformation of the Nazca Plate: New constraints from GPS measurements. *Geophysical Journal International*, *232*(2), 842–863. https://doi.org/10.1093/gji/ggac353

Jiang, Y., Samsonov, S. V., & González, P. J. (2022). Aseismic fault slip during a shallow normal-faulting seismic swarm constrained using a physically informed geodetic inversion method. *Journal of Geophysical Research: Solid Earth*, *127*(7), e2021JB022621. https://doi.org/10.1029/2021JB022621

Johnson, K., Villani, M., Bayliss, K., Brooks, C., Chandrasekhar, S., Chartier, T., et al. (2023). Global seismic hazard map. https://doi.org/10.5281/zenodo.10034133

Jolivet, R., & Simons, M. (2018). A multipixel time series analysis method accounting for ground motion, atmospheric noise, and orbital errors. *Geophysical Research Letters*, *45*(4), 1814–1824. https://doi.org/10.1002/2017GL076533

Kadinsky-Cade, K., Reilinger, R., & Isacks, I. (1985). Surface deformation associated with the November 23, 1977, Caucete, Argentina earthquake sequence. *Journal of Geophysical Research*, *90*(B14), 12691–12700. https://doi.org/10.1029/JB090IB14P12691

Kley, J., & Monaldi, C. R. (1998). Tectonic shortening and crustal thickness in the Central Andes: How good is the correlation? *Geology*, *26*(8), 723–726. https://doi.org/10.1130/0091-7613(1998)026<0723:TSACTI>2.3.CO;2

Kley, J., Monaldi, C. R., & Salfity, J. A. (1999). Along-strike segmentation of the Andean foreland: Causes and consequences. *Tectonophysics*, *301*(1–2), 75–94. https://doi.org/10.1016/S0040-1951(98)90223-2

Kley, J., Rossello, E. A., Monaldi, C. R., & Habighorst, B. (2005). Seismic and field evidence for selective inversion of Cretaceous normal faults, Salta rift, northwest Argentina. *Tectonophysics*, *399*(1–4), 155–172. https://doi.org/10.1016/J.TECTO.2004.12.020

Knight, E. (2023). *The kinematics and dynamics of active mountain ranges*. University of Cambridge. https://doi.org/10.17863/CAM.105931

Kostrov, V. V. (1974). Seismic moment and energy of earthquakes, and seismic flow of rock. *Earth Physics*, *1*, 23–40.

Koulakov, I., Sobolev, S. V., & Asch, G. (2006). P- and S-velocity images of the lithosphere—Asthenosphere system in the Central Andes from local-source tomographic inversion. *Geophysical Journal International*, *167*(1), 106–126. https://doi.org/10.1111/J.1365-246X.2006.02949.X

La Femina, P. C., Dixon, T. H., & Strauch, W. (2002). Bookshelf faulting in Nicaragua. *Geology*, *30*(8), 751–754. https://doi.org/10.1130/0091-7613(2002)030<0751:BFIN>2.0.CO;2

Lamb, S. (2000). Active deformation in the Bolivian Andes, South America. *Journal of Geophysical Research*, *105*(B11), 25627–25653. https://doi.org/10.1029/2000JB900187

Lazeckỳ, M., Spaans, K., González, P. J., Maghsoudi, Y., Morishita, Y., Albino, F., et al. (2020). LiCSAR: An automatic InSAR tool for measuring and monitoring tectonic and volcanic activity. *Remote Sensing*, *12*(15), 2430. https://doi.org/10.3390/RS12152430

León-Ibáñez, P., & Delgado, F. (2025). Resolving blind mid-crustal earthquake deformation with InSAR time-series: The 2021 M w 6.4 San Juan earthquake and implications for a non-optimal fault reactivation in the Andean fold and thrust belt, Argentina. *Geophysical Journal International*, *243*, 1–16. https://doi.org/10.1093/gji/ggaf394

Leroy, N., Vallée, M., Zigone, D., Romanowicz, B., Stutzmann, E., Maggi, A., et al. (2024). GEOSCOPE network: 40 Yr of global broadband seismic data. *Seismological Research Letters*, *95*(3), 1495–1517. https://doi.org/10.1785/0220230176

Li, X., Hergert, T., Henk, A., Wang, D., & Zeng, Z. (2019). Subsurface structure and spatial segmentation of the Longmen Shan fault zone at the eastern margin of Tibetan Plateau: Evidence from focal mechanism solutions and stress field inversion. *Tectonophysics*, *757*, 10–23. https://doi.org/10.1016/J.TECTO.2019.03.006

Liu, F., Elliott, J. R., Craig, T. J., Hooper, A., & Wright, T. J. (2021). Improving the resolving power of InSAR for earthquakes using time series: A case study in Iran. *Geophysical Research Letters*, *48*(14), e2021GL093043. https://doi.org/10.1029/2021GL093043

Lohman, R. B., & Barnhart, W. D. (2010). Evaluation of earthquake triggering during the 2005–2008 earthquake sequence on Qeshm Island, Iran. *Journal of Geophysical Research*, *115*(B12), 12413. https://doi.org/10.1029/2010JB007710

Luo, H., Wang, T., Wei, S., Liao, M., & Gong, J. (2021). Deriving centimeter-level coseismic deformation and fault geometries of small-to-moderate earthquakes from time-series sentinel-1 SAR images. *Frontiers in Earth Science*, *9*, 636398. https://doi.org/10.3389/feart.2021.636398

Marconato, L., Audin, L., Doin, M.-P., Nocquet, J.-M., Jarrin, P., Rolandone, F., et al. (2024). Internal deformation of the North Andean sliver in Ecuador-southern Colombia observed by InSAR. *Geophysical Journal International*, ggae338. https://doi.org/10.1093/GJI/GGAE338

Marrett, R. A., Allmendinger, R. W., Alonso, R. N., & Drake, R. E. (1994). Late Cenozoic tectonic evolution of the Puna Plateau and adjacent foreland, northwestern Argentine Andes. *Journal of South American Earth Sciences*, *7*(2), 179–207. https://doi.org/10.1016/0895-9811(94)90007-8

McCaffrey, R., & Abers, G. (1988). SYN3, a program for inversion of teleseismic body wave forms on microcomputers. *Force Geophysics Laboratory, Air Force Systems Command, US Air Force*.

McFarland, P. K., Bennett, R. A., Alvarado, P., & DeCelles, P. G. (2017). Rapid geodetic shortening across the eastern Cordillera of NW Argentina observed by the Puna-Andes GPS array. *Journal of Geophysical Research: Solid Earth*, *122*(10), 8600–8623. https://doi.org/10.1002/2017JB014739

Meigs, A. J., & Nabelek, J. (2010). Crustal-scale pure shear foreland deformation of western Argentina. *Geophysical Research Letters*, *37*(11), 11304. https://doi.org/10.1029/2010GL043220

Molnar, P., & Lyon-Caen, H. (1988). Some simple physical aspects of the support, structure, and evolution of mountain belts. *Special Papers - Geological Society of America*, *218*, 179–207. https://doi.org/10.1130/SPE218-P179

Molnar, P., & Lyon-Caen, H. (1989). Fault plane solutions of earthquakes and active tectonics of the Tibetan Plateau and its margins. *Geophysical Journal International*, *99*(1), 123–154. https://doi.org/10.1111/j.1365-246X.1989.tb02020.x

Morishita, Y., Lazecky, M., Wright, T. J., Weiss, J. R., Elliott, J. R., & Hooper, A. (2020). LiCSBAS: An open-source insar time series analysis package integrated with the LiCSAR automated sentinel-1 InSAR processor. *Remote Sensing*, *12*(3), 424. https://doi.org/10.3390/rs12030424

Murphy, M. A., Taylor, M. H., Gosse, J., Silver, C. R., Whipp, D. M., & Beaumont, C. (2014). Limit of strain partitioning in the Himalaya marked by large earthquakes in western Nepal. *Nature Geoscience*, *7*(1), 38–42. https://doi.org/10.1038/ngeo2017

Nabelek, J. L. (1984). Determination of earthquake source parameters from inversion of body waves. *M. I. T., Department of Earth, Atmospheric and Planetary Sciences*.

Nissen, E., Tatar, M., Jackson, J. A., & Allen, M. B. (2011). New views on earthquake faulting in the Zagros fold-and-thrust belt of Iran. *Geophysical Journal International*, *186*, 928–944. https://doi.org/10.1111/j.1365-246X.2011.5119.x

Nocquet, J. M., Villegas-Lanza, J. C., Chlieh, M., Mothes, P. A., Rolandone, F., Jarrin, P., et al. (2014). Motion of continental slivers and creeping subduction in the northern Andes. *Nature Geoscience*, *7*(4), 287–291. https://doi.org/10.1038/ngeo2099

Okada, Y. (1985). Surface deformation due to shear and tensile faults in a half-space. *Bulletin of the Seismological Society of America*, *75*(4), 1135–1154. https://doi.org/10.1785/BSSA0750041135

Orrego, S., Biggs, J., Wimpenny, S., & Maghsoudi, Y. (2025). Codes used in "Range-parallel extension of the Andes in the 2020 Mw 5.7 Humahuaca earthquake" [Software]. *Zenodo*. https://doi.org/10.5281/zenodo.15658649

Petersen, M. D., Harmsen, S. C., Jaiswal, K. S., Rukstales, K. S., Luco, N., Haller, K. M., et al. (2018). Seismic hazard, risk, and design for South America. *Bulletin of the Seismological Society of America*, *108*(2), 781–800. https://doi.org/10.1785/0120170002

Pritchard, M. E., Ji, C., & Simons, M. (2006). Distribution of slip from 11 M_w>6 earthquakes in the northern Chile subduction zone. *Journal of Geophysical Research*, *111*(10). https://doi.org/10.1029/2005JB004013

Quinteros, J., Strollo, A., Evans, P. L., Hanka, W., Heinloo, A., Hemmleb, S., et al. (2021). The GEOFON program in 2020. *Seismological Research Letters*, *92*(3), 1610–1622. https://doi.org/10.1785/0220200415

Ryder, I., Bürgmann, R., & Sun, J. (2010). Tandem afterslip on connected fault planes following the 2008 Nima-Gaize (Tibet) earthquake. *Journal of Geophysical Research*, *115*(B3), 3404. https://doi.org/10.1029/2009JB006423

Schoenbohm, L. M., & Strecker, M. R. (2009). Normal faulting along the southern margin of the Puna Plateau, northwest Argentina. *Tectonics*, *28*(5). https://doi.org/10.1029/2008TC002341

Schurr, B., Asch, G., Rietbrock, A., Kind, R., Pardo, M., Heit, B., & Monfret, T. (1999). Seismicity and average velocities beneath the Argentine Puna Plateau. *Geophysical Research Letters*, *26*(19), 3025–3028. https://doi.org/10.1029/1999GL005385

Schurr, B., Ratschbacher, L., Sippl, C., Gloaguen, R., Yuan, X., & Mechie, J. (2014). Seismotectonics of the Pamir. *Tectonics*, *33*(8), 1501–1518. https://doi.org/10.1002/2014TC003576

Shea, H. N., & Barnhart, W. D. (2022). The geodetic centroid (gCent) catalog: Global earthquake monitoring with satellite imaging geodesy. *Bulletin of the Seismological Society of America*, *112*(6), 2946–2957. https://doi.org/10.1785/0120220072

Siks, B. C., & Horton, B. K. (2011). Growth and fragmentation of the Andean foreland basin during eastward advance of fold-thrust deformation, Puna plateau and Eastern Cordillera, northern Argentina. *Tectonics*, *30*(6). https://doi.org/10.1029/2011TC002944

Styron, R. H., Taylor, M. H., & Murphy, M. A. (2011). Oblique convergence, arc-parallel extension, and the role of strike-slip faulting in the high Himalaya. *Geosphere*, *7*(2), 582–596. https://doi.org/10.1130/GES00606.1

Tapponnier, P., Mercier, J. L., Armijo, R., Tonglin, H., & Ji, Z. (1981). Field evidence for active normal faulting in Tibet. *Nature*, *294*(5840), 410–414. https://doi.org/10.1038/294410a0

Taymaz, T., Jackson, J., & Westaway, R. (1990). Earthquake mechanisms in the Hellenic trench near Crete. *Geophysical Journal International*, *102*(3), 695–731. https://doi.org/10.1111/J.1365-246X.1990.TB04590.X

Tian, D., Uieda, L., Leong, W. J., Fröhlich, Y., Schlitzer, W., Grund, M., et al. (2024). PyGMT: A Python interface for the generic mapping tools. https://doi.org/10.5281/zenodo.13679420

van Kooten, W. S., Vallati, M., Sobel, E. R., del Papa, C. E., Payrola, P., Starck, D., et al. (2024). Structural inheritance in the Eastern Cordillera, NW Argentina: Low-temperature thermochronology of the Cianzo Basin. *Tectonics*, *43*(6), e2023TC007949. https://doi.org/10.1029/2023TC007949

Watts, A. B., Lamb, S. H., Fairhead, J. D., & Dewey, J. F. (1995). Lithospheric flexure and bending of the Central Andes. *Earth and Planetary Science Letters*, *134*(1–2), 9–21. https://doi.org/10.1016/0012-821X(95)00095-T

Weiss, J. R., Brooks, B. A., Foster, J. H., Bevis, M., Echalar, A., Caccamise, D., et al. (2016). Isolating active orogenic wedge deformation in the southern Subandes of Bolivia. *Journal of Geophysical Research: Solid Earth*, *121*(8), 6192–6218. https://doi.org/10.1002/2016JB013145

Wessel, P., Luis, J. F., Uieda, L., Scharroo, R., Wobbe, F., Smith, W. H., & Tian, D. (2019). The generic mapping tools version 6. *Geochemistry, Geophysics, Geosystems*, *20*(11), 5556–5564. https://doi.org/10.1029/2019GC008515

Weston, J., Ferreira, A. M., & Funning, G. J. (2012). Systematic comparisons of earthquake source models determined using InSAR and seismic data. *Tectonophysics*, *532–535*, 61–81. https://doi.org/10.1016/j.tecto.2012.02.001

Weston, J., Ferreira, A. M., & Funning, G. J. (2014). Joint earthquake source inversions using seismo-geodesy and 3-D Earth models. *Geophysical Journal International*, *198*(2), 671–696. https://doi.org/10.1093/gji/ggu110

Wimpenny, S., Benavente, C., Copley, A., Garcia, B., Rosell, L., O'Kane, A., & Aguirre, E. (2020). Observations and dynamical implications of active normal faulting in South Peru. *Geophysical Journal International*, *222*(1), 27–53. https://doi.org/10.1093/gji/ggaa144

Wimpenny, S., Copley, A., Benavente, C., & Aguirre, E. (2018). Extension and dynamics of the Andes inferred from the 2016 Parina (Huarichancara) earthquake. *Journal of Geophysical Research: Solid Earth*, *123*(9), 8198–8228. https://doi.org/10.1029/2018JB015588

Wimpenny, S., & Watson, C. S. (2020). gWFM: A global catalog of moderate-magnitude earthquakes studied using teleseismic body waves. *Seismological Research Letters*, *92*(1), 212–226. https://doi.org/10.1785/0220200218

Woodcock, N. H., & Fischer, M. (1986). Strike-slip duplexes. *Journal of Structural Geology*, *8*(7), 725–735. https://doi.org/10.1016/0191-8141(86)90021-0

Yang, J., Xu, C., Wen, Y., & Xu, G. (2022). Complex coseismic and postseismic faulting during the 2021 Northern Thessaly (Greece) earthquake sequence illuminated by InSAR observations. *Geophysical Research Letters*, *49*(8), e2022GL098545. https://doi.org/10.1029/2022GL098545

Yu, C., Li, Z., Chen, J., & Hu, J. C. (2018). Small magnitude co-seismic deformation of the 2017 Mw 6.4 Nyingchi earthquake revealed by InSAR measurements with atmospheric correction. *Remote Sensing*, *10*(5), 684. https://doi.org/10.3390/RS10050684

Yu, C., Li, Z., Penna, N. T., & Crippa, P. (2018). Generic atmospheric correction model for interferometric synthetic aperture radar observations. *Journal of Geophysical Research: Solid Earth*, *123*(10), 9202–9222. https://doi.org/10.1029/2017JB015305

Zhang, Y., Shan, X., Gong, W., & Zhang, G. (2021). The ambiguous fault geometry derived from InSAR measurements of buried thrust earthquakes: A synthetic data based study. *Geophysical Journal International*, *225*(3), 1799–1811. https://doi.org/10.1093/gji/ggab021

Zheng, G., Wang, H., Wright, T. J., Lou, Y., Zhang, R., Zhang, W., et al. (2017). Crustal deformation in the India-Eurasia collision zone from 25 years of GPS measurements. *Journal of Geophysical Research: Solid Earth*, *122*(11), 9290–9312. https://doi.org/10.1002/2017JB014465

Zhou, R., Schoenbohm, L. M., & Cosca, M. (2013). Recent, slow normal and strike-slip faulting in the Pasto Ventura region of the southern Puna Plateau, NW Argentina. *Tectonics*, *32*(1), 19–33. https://doi.org/10.1029/2012TC003189

Zhou, Y., Thomas, M. Y., Parsons, B., & Walker, R. T. (2018). Time-dependent postseismic slip following the 1978 Mw 7.3 Tabas-e-Golshan, Iran earthquake revealed by over 20 years of ESA InSAR observations. *Earth and Planetary Science Letters*, *483*, 64–75. https://doi.org/10.1016/J.EPSL.2017.12.005

Zubovich, A., Schöne, T., Metzger, S., Mosienko, O., Mukhamediev, S., Sharshebaev, A., & Zech, C. (2016). Tectonic interaction between the Pamir and Tien Shan observed by GPS. *Tectonics*, *35*(2), 283–292. https://doi.org/10.1002/2015TC004055

Zwick, P., McCaffrey, R., & Abers, G. (1994). MT5 program.